https://ntrs.nasa.gov/search.jsp?R=20190002028 2020-05-09T12:43:40+00:00Z

AGU100 ADVANCING EARTH AND SPACE SCIENCE

JAMES Journal of Advances in Modeling Earth Systems

RESEARCH ARTICLE
10.1029/2018MS001443

Key Points:
- Resolved vertical turbulent fluxes remain important for length scales up to 10 km
- Smagorinsky-type TKE subgrid models have some desired scale-aware properties
- Cloud transition is strongly controlled by the prescribed cloud droplet number concentration and details of the ice microphysics scheme

Correspondence to:
S. R. de Roode,
s.r.deroode@tudelft.nl

Citation:
de Roode, S. R., Frederikse, T., Siebesma, A. P., Ackerman, A. S., Chylik, J., Field, P. R., et al. (2019). Turbulent transport in the gray zone: A large eddy model intercomparison study of the CONSTRAIN cold air outbreak case. *Journal of Advances in Modeling Earth Systems*, *11*. https://doi.org/10.1029/2018MS001443

Received 16 JUL 2018
Accepted 7 FEB 2019
Accepted article online 9 FEB 2019

©2019. The Authors.
This is an open access article under the terms of the Creative Commons Attribution-NonCommercial-NoDerivs License, which permits use and distribution in any medium, provided the original work is properly cited, the use is non-commercial and no modifications or adaptations are made.

Turbulent Transport in the Gray Zone: A Large Eddy Model Intercomparison Study of the CONSTRAIN Cold Air Outbreak Case

Stephan R. de Roode[1], Thomas Frederikse[1], A. Pier Siebesma[1], Andrew S. Ackerman[2], Jan Chylik[3], Paul R. Field[4], Jens Fricke[5], Micha Gryschka[5], Adrian Hill[4], Rachel Honnert[6], Steve K. Krueger[7], Christine Lac[6], Andrew T. Lesage[7], and Lorenzo Tomassini[4,8]

[1]Department of Geosciences and Remote Sensing, Faculty of Civil Engineering and Geosciences, Delft University of Technology, Delft, Netherlands, [2]NASA Goddard Institute for Space Studies, New York, NY, USA, [3]Institute for Geophysics and Meteorology, Department of Geosciences, University of Cologne, Cologne, Germany, [4]U.K. Meteorological Office, Exeter, UK, [5]Institut für Meteorologie und Klimatologie, Leibniz Universität, Hannover, Germany, [6]Meteo-France, Toulouse, France, [7]Department of Atmospheric Sciences, University of Utah, Salt Lake City, UT, USA, [8]Max PIanck Institute for Meteorology, Hamburg, Germany

Abstract To quantify the turbulent transport at gray zone length scales between 1 and 10 km, the Lagrangian evolution of the CONSTRAIN cold air outbreak case was simulated with seven large eddy models. The case is characterized by rather large latent and sensible heat fluxes mention the meaning of SHF in the text below and remove from abstract and a rapid deepening rate of the boundary layer. In some models the entrainment velocity exceeds 4 cm/s. A significant fraction of this growth is attributed to a strong longwave radiative cooling of the inversion layer. The evolution and the timing of the breakup of the stratocumulus cloud deck differ significantly among the models. Sensitivity experiments demonstrate that a decrease in the prescribed cloud droplet number concentration and the inclusion of ice microphysics both act to speed up the thinning of the stratocumulus by enhancing the production of precipitation. In all models the formation of mesoscale fluctuations is clearly evident in the cloud fields and also in the horizontal wind velocity. Resolved vertical fluxes remain important for scales up to 10 km. The simulation results show that the resolved vertical velocity variance gradually diminishes with a coarsening of the horizontal mesh, but the total vertical fluxes of heat, moisture, and momentum are only weakly affected. This is a promising result as it demonstrates the potential use of a mesh size-dependent turbulent length scale for convective boundary layers at gray zone model resolutions.

1. Introduction

Parameterization schemes for boundary layer turbulence and convective clouds in large-scale models have been designed traditionally on the basis of the assumption that vertical transport of properties like heat, moisture, and momentum occurs entirely at subgrid scales. But now the ever increasing computational power allows operation of numerical weather prediction models at so-called "gray zone" resolutions (Wyngaard, 2004) at horizontal grid spacings as fine as 1 km, in which the horizontal grid spacing is sufficient to capture some fraction of the convective transport that occurs at horizontal scales up to about 10 km (Field et al., 2017). Consequently, parameterizations will need to be modified to smoothly blend resolved and subgrid-scale contributions (Arakawa et al., 2011).

Mesoscale fluctuations are frequently observed in boundary layer clouds such as stratocumulus (Wood & Hartmann, 2006). The Working Group on Numerical Experimentation of the World Climate Research Programme selected the CONSTRAIN cold air outbreak (CAO) case (Field et al., 2014) as a framework to test the behavior of global models and limited area weather forecast models operating in, or close to, gray zone resolutions.

In a CAO a stratocumulus cloud deck is advected over an increasingly warmer sea surface temperature (SST), causing a deepening of the boundary layer and the formation of shallow cumulus clouds underneath the stratocumulus. A CAO is a specific example of a larger class of stratocumulus to shallow cumulus transitions (SCTs), another variant of which is a climatological feature over the subtropical oceans, and

SCTs are perhaps the most challenging boundary layer regime to be represented by large-scale models (Neggers et al., 2017). SCTs are controlled by a wide variety of physical processes. If the stratocumulus cloud layer is sufficiently thick, and if the overlying atmosphere is clear, the stratocumulus will emit more infrared radiation than it absorbs from above, which yields a strong cooling of the cloud top that produces turbulence by the formation of negatively buoyant downdrafts (Duynkerke et al., 1995). Turbulence causes some mixing of relatively warm and dry air from across the capping thermal inversion. This process, which is referred to as cloud top entrainment, is one of the key processes that causes a thinning tendency of the stratocumulus cloud layer (Stage & Businger, 1981; Stevens, 2002; Van der Dussen et al., 2014). Rain formation is another process that leads to the depletion of cloud water. If the precipitation is sufficiently strong, this may ultimately lead to the formation of open cells (Wang & Feingold, 2009). A striking feature of CAOs is the presence of so-called cloud streets (e.g., Brümmer, 1999; Gryschka & Raasch, 2005), which organization is controlled by the ratio of shear to buoyancy production of turbulent kinetic energy (TKE) in a nontrivial way.

Tomassini et al. (2017) investigated the representation of the CONSTRAIN CAO in global models. In particular, they assessed to what extent current convection and boundary layer parameterizations behave in a scale-adaptive manner in situations where the horizontal grid spacing of global models approaches the scale of convection. They found that even at the highest grid resolution of 1 km used in a nested domain, simulations with convective parameterizations do not converge toward the results of simulations without such parameterizations. In an accompanying study using limited area models (LAMs) by Field et al. (2017) it was concluded that stratocumulus cloud amount is underestimated in the CONSTRAIN CAO case, which is a well-known bias in large-scale models (Richter, 2015).

Large eddy simulation (LES) models are well capable of capturing the observed SCT in the subtropics (De Roode et al., 2016; Van der Dussen et al., 2013). In addition, Honnert et al. (2011), Dorrestijn et al. (2013), and Shin and Hong (2013) demonstrated that the partitioning of the subgrid and resolved turbulent transports as a function of horizontal grid spacing can be well diagnosed from turbulence resolving LES models. Motivated by these studies, we performed a similar analysis using results of the CONSTRAIN CAO case as obtained from seven different LES models. They all used a horizontal domain that is sufficiently large to allow the development of fluctuations at scales larger than a few kilometers, at the so-called mesoscales (Bretherton & Blossey, 2017; De Roode et al., 2004; Jonker et al., 1999; Müller & Chlond, 1996; Savic-Jovcic & Stevens, 2008). For computational efficiency, the horizontal resolution is set to 250 m following Wang and Feingold (2009), who found that this somewhat coarse horizontal resolution does not have a significant impact on the cellular structures. At this grid resolution, simulations are sometimes referred to as large eddy permitting (Green & Zhang, 2015) or simply eddy permitting (Nakamura et al., 2012). Some additional simulations were performed to assess the performance of LES subgrid models for horizontal grid spacings that are typically used by high-resolution regional weather forecast models (>1 km). This was done with a traditional prognostic subgrid TKE model. As it has been shown by Cheng and Xu (2008) that a higher-order closure subgrid model may be well used to simulate cumulus and stratocumulus for horizontal grid spacing up to 4 km, simulations with a higher-order closure model for the subgrid fluxes and variances (Bogenschutz & Krueger, 2013) were performed with one model.

The LES results are used to address the following questions. How does the boundary layer in the CAO evolve in time in terms of the mean state and turbulence structure and how does it compare to the subtropical SCT? What is impact of drizzle production on the maintenance of the stratocumulus cloud layer? How large are the maximum length scales of the vertical turbulent transport? How does LES perform if a coarse horizontal grid spacing is applied that is typical for a high-resolution limited area weather forecast model? The setup of the case and the participating models are presented in section 2. In section 3 the results of the reference case are discussed. Section 4 diagnoses how the resolved and subgrid fluxes should be partitioned as a function of an assumed applied mesh size Dx such as used in a large-scale model. Sensitivity studies addressing cloud microphysics in terms of the effects of the prescribed value for the cloud droplet number concentration and ice microphysics are discussed in section 5. Section 6 discusses the LES runs that were performed with a coarse horizontal mesh size, and section 7 summarizes the main findings.

2. Setup of the Experiments

2.1. Initial, Boundary, and Large-Scale Forcing Conditions

The proposed CAO case is a Lagrangian experiment, in which the model domain is advected by a south-southeasterly wind from a latitude (longitude) of 66(−11)° to 60(−8.7)°. The start time for the simulations is 00 UTC on 31 January 2010. Initial conditions for the case are based on high-resolution LAM

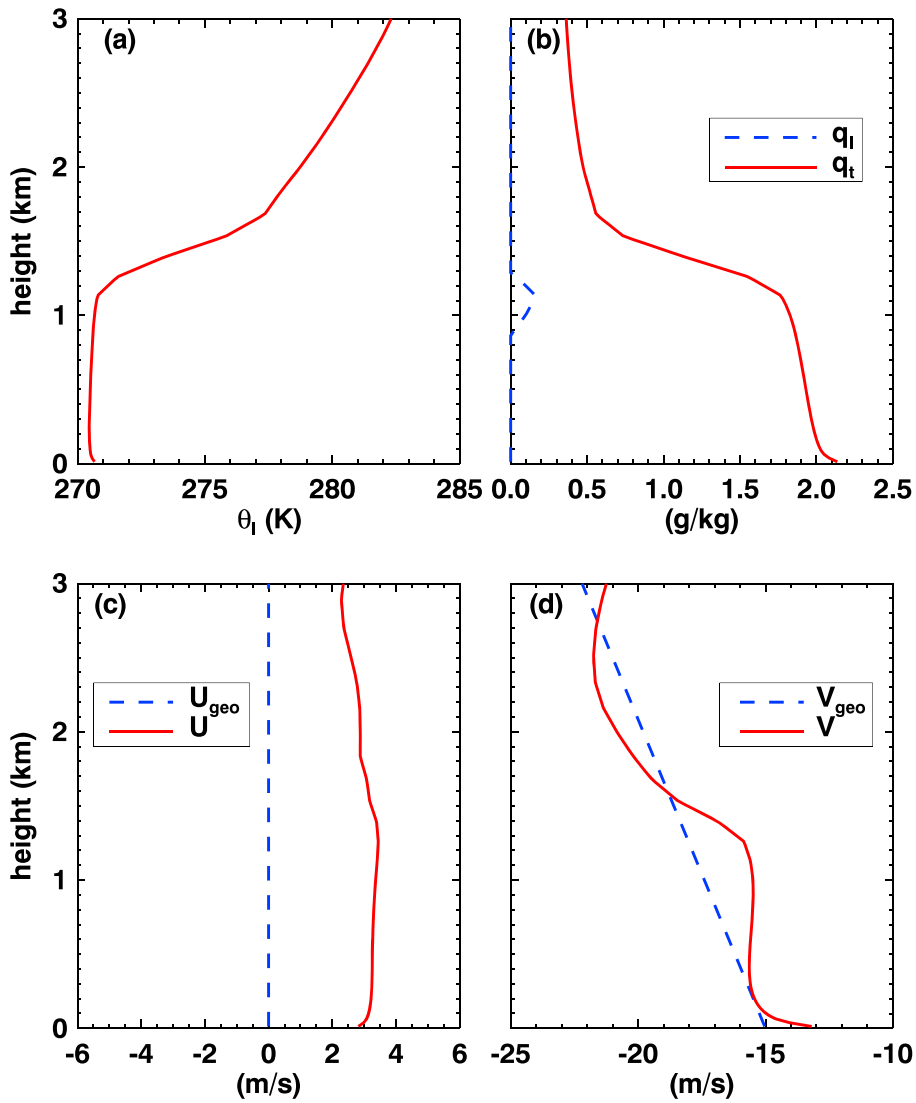

Figure 1. The prescribed initial vertical profiles for (a) θ_l, (b) q_l and q_t, and (c) the zonal and (d) meridional wind speeds including their geostrophic values. Line styles are according to the legends.

simulations performed with the Met Office Unified Model (Field et al., 2014). Initial thermodynamic vertical profiles up to a height of 38 km are provided. Figure 1 shows the initial conditions of the zonal (u) and meridional (v) winds, the liquid water potential temperature ($\theta_l = \theta - \frac{L_v}{c_p}\frac{\theta}{T}q_l$), total water specific humidity defined by the sum of water vapor (q_v), cloud liquid water (q_l), rain (q_r), and total ice (q_i). Here θ denotes the potential temperature, L_v is the latent heat of vaporization, c_p is the specific heat of dry air at constant pressure, and T is the temperature. Note that we will use the variable $q_t = q_v + q_l$ to denote the total water specific humidity in warm clouds excluding rain. These initial conditions were all diagnosed from the Unified Model at the beginning of the Lagrangian track.

The initial wind conditions are characterized by a strong meridional component (12 to 17 m/s in the boundary layer) and a substantially weaker zonal component (3 to 4 m/s). The geostrophic wind is constant in time. The zonal geostrophic wind speed u_{geo} is 0, and the meridional component v_{geo} depends on the height z according to

$$v_{geo} \equiv -\frac{1}{\rho f}\frac{\partial p}{\partial y} = -15 - 0.0024z. \tag{1}$$

Here f is the Coriolis parameter ($1.3 \cdot 10^{-4}$ s^{-1} at a latitude of 63°), ρ the density of air, and p the pressure. The factor 0.0024 has units of per second. The geostrophic wind deviates from the actual initial wind conditions

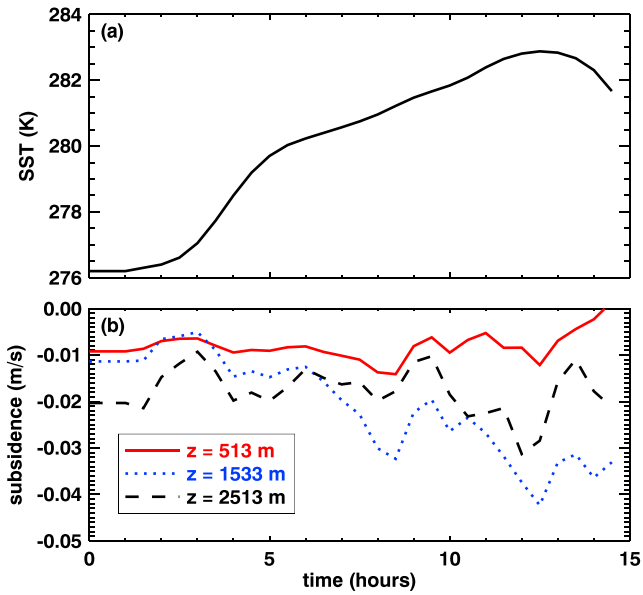

Figure 2. The prescribed time-dependent (a) sea surface temperature (SST) and (b) large-scale subsidence at three heights.

which results in a net force. Because during the spin-up phase the momentum fluxes may evolve quite differently among the LES models, differences in sign of the tendencies of the horizontal wind velocity components may develop. This is elaborated in the appendix.

The case is run for 14.5 hr, in which the first 1.5 hr represent a spin-up using a fixed surface temperature. After this spin-up period the surface is forced using a prescribed time-varying SST that represents the advection of the air mass over an increasingly warmer sea surface until the final hour (see Figure 2a). Figure 2b shows the time-varying large-scale subsidence at three representative heights. The simulations apply the following settings for the roughness length for momentum and scalars, $z_0 = 6.6 \cdot 10^{-4}$ m and $z_T = 3.7 \cdot 10^{-6}$ m, respectively. The surface pressure is a constant 1,009 hPa.

The aircraft observations collected in the southern, cumulus dominated part of the observations indicated very small cloud droplet number concentration N_c of about 10 cm^{-3} (Field et al., 2017). Unfortunately, there were no observations of N_c in the earlier stratocumulus stage of the case. The reference case simulations were performed without ice microphysics. Furthermore, a fixed value for N_c of 50 cm^{-3} was prescribed. The sensitivity of the results to ice microphysics and N_c was explored in additional sensitivity runs. The interactive radiation scheme uses a standard midlatitude winter McClatchy ozone profile.

2.2. Participating LES Models

In total, seven LES models participated in this study. The details on the model formulations and the used microphysics schemes can be found in the references presented in Table 1. Some details regarding the microphysics scheme of Seifert and Beheng (2006) will be discussed in the section on ice microphysics. Here we will briefly summarize some variants of widely used subgrid models. In LES models the subgrid fluxes for the filtered momentum and scalars, denoted here by a tilde, are computed following a downgradient diffusion approach:

$$\widetilde{u_j''\varphi''} = -K_h \frac{\partial \tilde{\varphi}}{\partial x_j}, \tag{2}$$

$$\widetilde{u_i''u_j''} = -K_m \left(\frac{\partial \tilde{u}_j}{\partial x_i} + \frac{\partial \tilde{u}_i}{\partial x_j} \right), \tag{3}$$

where double primes indicate subgrid fluctuations. Single primes will be used to indicate the fluctuation of a quantity with respect to a horizontal mean value. The eddy viscosity K_m and diffusivity K_h are defined as, respectively,

$$K_{m,h} = c_{m,h} \lambda \tilde{e}^{1/2}. \tag{4}$$

The proportionality factors c_m and c_h are coupled through the turbulent Prandtl number, $Pr \equiv c_m/c_h$. As discussed by De Roode et al. (2017) there is no widely accepted value for Pr, and in practice values between 1/3 and 1 are used.

DALES, SAM, Meso-NH, and PALM solve the prognostic equation for the subgrid TKE $\tilde{e} = \widetilde{u_i''u_i''}$:

$$\frac{d\tilde{e}}{dt} = \frac{g}{\theta_0}\widetilde{w''\theta_v''} - \widetilde{u_i''u_j''}\frac{\partial \tilde{u}_i}{\partial x_j} - \frac{\partial \widetilde{u_i''u_i''u_j''}}{\partial x_j} - \frac{1}{\rho_0}\frac{\partial \widetilde{u_j''p''}}{\partial x_j} - \epsilon, \tag{5}$$

with ρ_0 a reference density and p the pressure. The total turbulent transport term is computed following a downgradient diffusion approach:

$$\widetilde{u_i''u_i''u_j''} + \frac{\widetilde{u_j''p''}}{\rho_0} = -2K_m \frac{\partial \tilde{e}}{\partial x_j}. \tag{6}$$

Table 1
Summary of Participating Models

Institution	Model name	Modelers	Description	Microphysics
TU Delft	DALES	Frederikse and De Roode	Heus et al. (2010)	Seifert and Beheng (2006)
University of Cologne		Chylik		
MPI	UCLA-LES	Tomassini	Stevens et al. (2005)	Seifert and Beheng (2006)
UKMO	MONC	Hill	Dearden et al. (2018)	Morrison et al. (2005)
Leibniz University at Hannover	PALM	Fricke and Gryschka	Raasch and Schröter (2001) and Maronga et al. (2015)	Seifert and Beheng (2006)
Meteo-France	Meso-NH	Lac and Honnert	Lafore et al. (1997) and Lac et al. (2018)	Pinty and Jabouille (1998)
University of Utah	SAM	Lesage and Krueger	M. K. Khairoutdinov and Randall (2003)	M. K. Khairoutdinov and Randall (2003)
NASA	DHARMA	Ackerman	Kirkpatrick et al. (2006)	Morrison et al. (2005)

Note. DALES is the Dutch Atmospheric LES model. The University of Cologne has performed the ice microphysics runs with DALES. The Max-Planck Institute for Meteorology (MPI) uses the (University of California at Los Angeles) UCLA-LES model, the U.K. Meteorological Office (UKMO) runs the Meteorological Office Large Eddy Model, and the PArallelized Large Eddy Simulation Model for Atmospheric and Oceanic Flows (PALM) is operated by the Leibniz University at Hannover, Germany. Meteo-France has an LES incorporated in their mesocale nonhydrosotatic model Meso-NH. The University of Utah uses the System for Atmospheric Modeling (SAM). The National Aeronautics and Space Administration (NASA) runs the Distributed Hydrodynamic Aerosol and Radiation Modeling Application (DHARMA).

The viscous dissipation of $\tilde{e}$ by molecular viscosity (ϵ) is calculated as

$$\epsilon = c_\epsilon \frac{\tilde{e}^{3/2}}{\lambda}, \tag{7}$$

with c_ϵ a coefficient that is typically prescribed. The Smagorinsky-Lilly model, as applied by UCLA-LES, DHARMA, and MONC, is a simplified version of equation (5), which assumes a local balance between shear production, buoyancy, and dissipation of TKE. In DHARMA c_ϵ is not prescribed but instead is diagnosed on the basis of the local flow structure (Kirkpatrick et al., 2006).

The subgrid TKE model is closed by specifying the length scale λ. The mesh size-dependent length scale $\lambda = \Delta \equiv (\Delta x \Delta y \Delta z)^{1/3}$ was used by DALES, whereas UCLA-LES used a slightly different variant that attempts to match Monin-Obukhov similarity near the surface, $\lambda^{-2} = \Delta^{-2} + (z\kappa/c_s)^{-2}$, where κ is the von Karman constant and c_s the Smagorinsky constant. PALM and Meso-NH have applied the Deardorff (1980) length scale in which λ is equal to Δ, except for conditions of sufficiently strong local stable stratification according to

$$\lambda = \min\left(\Delta, c_n \frac{\tilde{e}^{1/2}}{N}\right), \tag{8}$$

with N the Brunt-Väisälä frequency and c_n a proportionality factor. Note that runs with DALES using the Deardorff length scale showed no significant differences as compared to runs with the constant length scale Δ. De Roode et al. (2017) presented analytical solutions of the Smagorinsky model in terms of the eddy viscosity and diffusivity for stably stratified conditions using any of the length scales summarized above.

The calculation of the subgrid TKE used in LES is analogous to what is used in some large-scale models (Bengtsson et al., 2017; Lac et al., 2018). The key difference is the formulation of the turbulent length scale, which in a large-scale model is taken to be representative for the characteristic boundary layer eddy size ℓ_{bl} that carry the bulk of the turbulent transport. Here it is interesting to mention that MONC uses $\lambda = (\Delta x + \Delta y + \Delta z)/3$, such that for strongly anisotropic grids as used in this study $\lambda \approx \Delta x$. By contrast, for SAM λ is set to Δz and the horizontal eddy-diffusion coefficients are computed by multiplying the vertical coefficients by a square of the ratio of horizontal to vertical grid spacings (Stevens et al., 2005).

Last, SAM has the option to run the model using the Simple Higher-Order Closure (SHOC) model presented by Bogenschutz and Krueger (2013). This closure computes the vertical fluxes and (co)variances of some key thermodynamic variables, which information serves as the subgrid-scale condensation scheme and

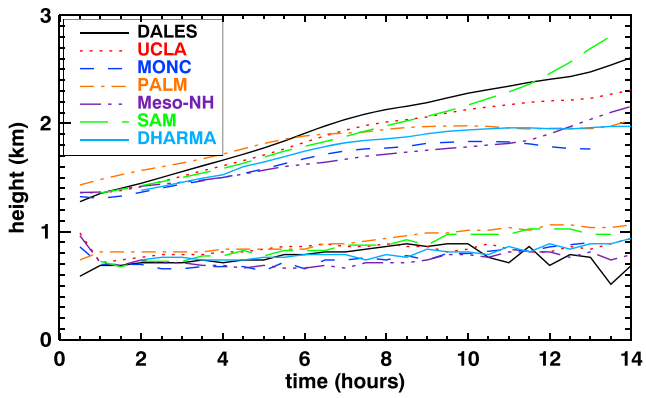

Figure 3. Reference case results for the minimum cloud base height and the mean cloud top height as diagnosed from half-hourly instantaneous 3-D fields. The presence of a cloud was detected by applying a threshold value for cloud liquid water, $q_l > 10^{-5}$ kg/kg. Line styles are according to the legend. The model names are given in Table 1.

turbulence closure. SHOC is scale aware in the sense larger grid spacings typically yield larger turbulent length scales through an implicit dependency on the subgrid-scale TKE.

2.3. Gray Zone Experiments

The simulations were performed on a horizontal domain size of 96 × 96 km^2. To limit the computational cost of the simulations, the models used a horizontal grid spacing of 250 m. The top of the LES domain was at 5 km, with a vertical grid spacing Δz of 25 m between the surface and 3 km. Above this height the vertical grid spacing at level k was coarsened according to $\Delta z^{k+1} = \alpha \Delta z^k$, with $\alpha = 1.02$ a stretch factor. This resulted in 47 extra levels above 3 km, so the total number level of vertical levels $k_{\max}$ was 167. Both the horizontal and vertical grid spacings were quite coarse, which is a trade-off to permit the large domain. The University of Utah (UU) used SAM and applied a finer horizontal grid spacing of 100 m but a somewhat smaller horizontal domain size of 64^2 km^2 and larger vertical grid spacing of 50 m in the boundary layer. In DALES the vertical grid was not stretched to avoid clouds penetrating into its sponge layer, which lowest level is located at a fixed fraction of the total number of vertical levels, $k = (3/4)k_{\max}$. For each numerical experiment 3-D fields were stored at intervals of 30 min. The simulations that excluded ice are referred to as the "reference" case simulations.

3. Reference Case Results

We first discuss the simulation results that were obtained for the reference case, which assumes a cloud layer without ice. The mean state evolution is analyzed in terms of the temporal evolution of the cloud deck. A couple of examples of vertical profiles of turbulent fluxes and variances are presented, and plots of some instantaneous horizontal fields will be shown to illustrate the development of mesoscale fluctuations. Except for the time series of the surface fluxes, all the results presented in this section were obtained from the instantaneous fields that were provided by the participants. The sensitivity experiments including variations in the cloud droplet number concentration N_c and ice microphysics will be discussed in section 5.

3.1. Time Series

Figure 3 presents the evolution of the cloud layer by means of the minimum cloud base height, which is representative for the lowest cumulus clouds, and the mean cloud top height. All models show a stratocumulus cloud deck whose top gradually rises during its southward advection. The lowest cloud base heights exhibit only relatively small changes in time. The Lagrangian evolution of a stratocumulus transition in a CAO therefore appears qualitatively similar to those in the subtropics in the sense that the cumulus cloud base height is almost in a steady state, while the stratocumulus cloud deck tends to rise during its advection over increasingly warmer SSTs (De Roode et al., 2016; Sandu et al., 2010). Aircraft data collected between 11 and 14 UTC indicate a broken cloud deck with cumulus cloud tops reaching heights up to 2.6 km (Field et al., 2014). This shows an important difference in the cloud top growth rate, which is much greater in this CAO than in subtropical SCTs.

The time series of various other quantities are shown in Figure 4. Here the liquid water path (LWP) is computed from the vertical integral of the horizontal mean liquid water specific humidity (excluding rain) times the air density. The MODIS image for 1200 UTC 31 January 2010 presented by Field et al. (2017, their Figure 1) shows an extensive field of broken clouds near the approximate final position of the Lagrangian trajectory. Figure 4a shows that in five LES models the cloud breaks up, with the UCLA-LES model exhibiting the smallest final cloud cover of about 0.86. It therefore appears that all models maintain a stratocumulus cloud deck, though most with some patches of clear air, which is notably different from the large-scale models, which tend to dissipate the stratocumulus cloud too rapidly (Field et al., 2017). The rain water path (RWP) values differ significantly among the models, both in terms of temporal evolution and magnitude. During the first part of the simulation DALES and SAM have the least RWP and both tend to maintain a closed stratocumulus cloud deck with significantly higher LWP values than the other models. There is a strong variability between the models in surface precipitation delete "and RWP" (this is already stated in the previous sentences). The surface sensible heat fluxes (SFHs) SHFs exceed values of 100 W/m^2,

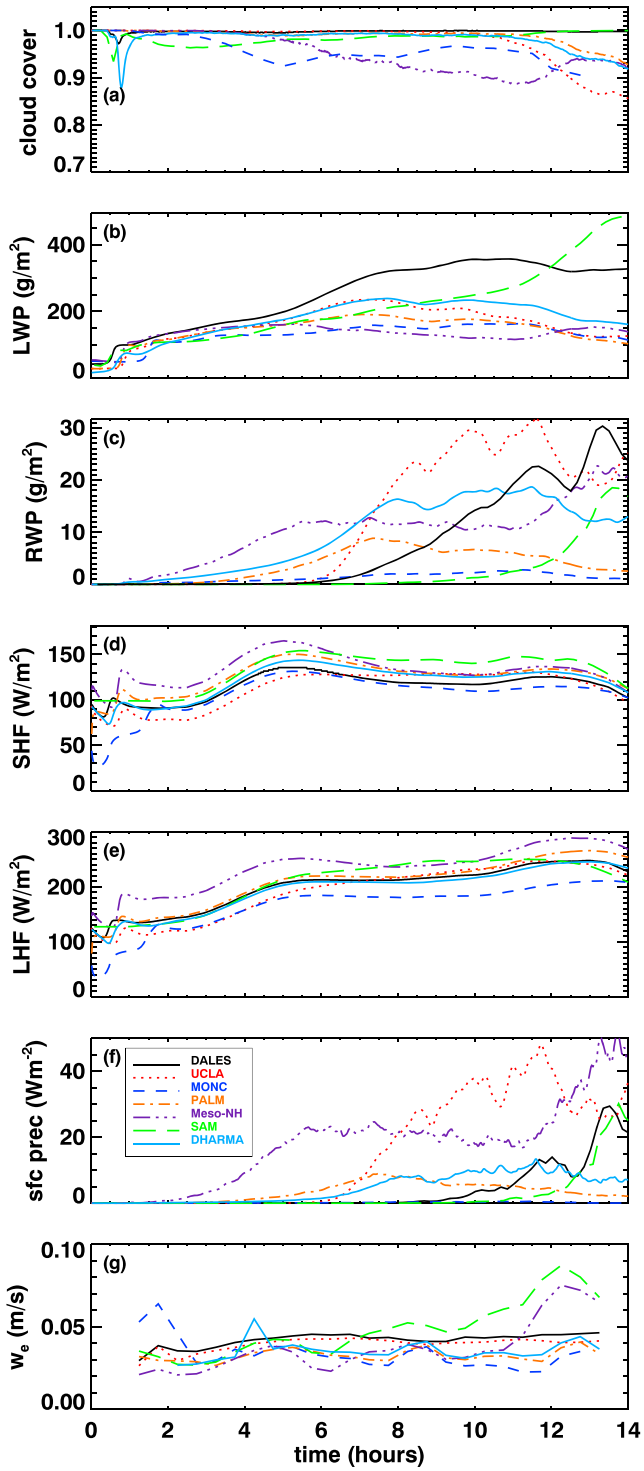

Figure 4. Time series for the reference case of (a) cloud cover, (b) cloud liquid water path (LWP), (c) rain water path (RWP), (d) sensible heat flux (SHF), (e) latent heat flux (LHF), (f) precipitation flux at the surface, and (g) entrainment velocity. Line styles are according to the legend. The model names are given in Table 1.

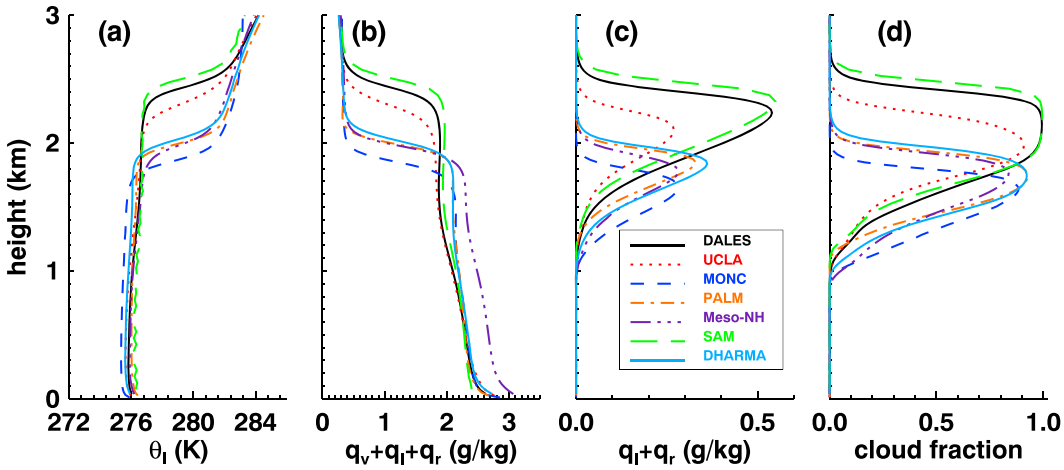

Figure 5. Reference case results of horizontal mean profiles of the instantaneous fields at $t = 12$ hr for (a) θ_l, (b) total water, (c) total cloud water, and (d) cloud fraction. Line styles are according to the legend. The model names are given in Table 1.

and the latent heat fluxes reach values that are about 200 W/m^2. The smaller fluxes for UKMO and MPI are related to their smaller wind speeds near the surface. The appendix explains how these differences arise erroneously during the spin-up phase of the simulations and are due to an initial wind that deviates from the geostrophic value. Meso-NH produces too strong heat surface fluxes. The problem is now well known and stems from the Louis (1979) parameterization for sea surface fluxes (Lebeaupin Brossier et al., 2008).

The LWP values start to diverge strongly after about 4 hr. The time series of the surface precipitation show differences in the timing and amounts of precipitation reaching the sea surface. They are somewhat smaller than the precipitation rates near the cloud base (not shown) due to the partial evaporation of rain in the subcloud layer. Since a rainfall flux of 30 W/m^2 corresponds to a LWP removal of about 43 g/m^2/hr , a large part of the differences that are found in the LWP tendencies can therefore be attributed to precipitation.

The entrainment rate w_e was diagnosed from the temporal change in the boundary layer depth (h) and the prescribed subsidence using mass conservation (Bretherton & Wyant, 1997):

$$w_e = \frac{dh}{dt} - \bar{w}|_h. \tag{9}$$

Figure 4g shows that all models give entrainment rates larger than 2 cm/s, with some having $w_e > 4$ cm/s. These entrainment rates are significantly larger than the values found in subtropical SCTs. For example, in the LES model intercomparison study by De Roode et al. (2016) four different subtropical SCTs were investigated. For the one that was based on observations collected during ASTEX (Atlantic Stratocumulus Transition Experiment), which had the weakest inversion stability of the four cases, a maximum value for the model-mean entrainment velocity of about 1.5 cm/s was found. In the next subsection it will be discussed that direct radiative cooling of the inversion layer plays an important role in the observed rapid growth of the boundary layer.

3.2. Thermodynamic Structure, Turbulence, and Longwave Radiation

An inspection of the vertical profiles of θ_l, total water, and total cloud water (see Figures 5a–5c) at $t = 12$ hr shows that all models maintain rather vertically well-mixed stratocumulus-topped boundary layers, with the subcloud layer only slightly moister and warmer (in terms of θ_l) than the cloud layer. This lack of stratification and the amount of cloud water are notable differences with the CONSTRAIN CAO results as obtained from large-scale models (Field et al., 2017). In this study it was suggested that the stratocumulus underestimation in the large-scale models could be alleviated if a well-mixed structure would be imposed. This notion appears to be supported by the LES model results. However, as compared to the observations from aircraft and satellite, the LES cloud cover results actually hint at a persistent stratocumulus cloud deck with rather high values for the cloud fraction, a feature that may be partly due to the neglect of ice microphysics in the reference case results.

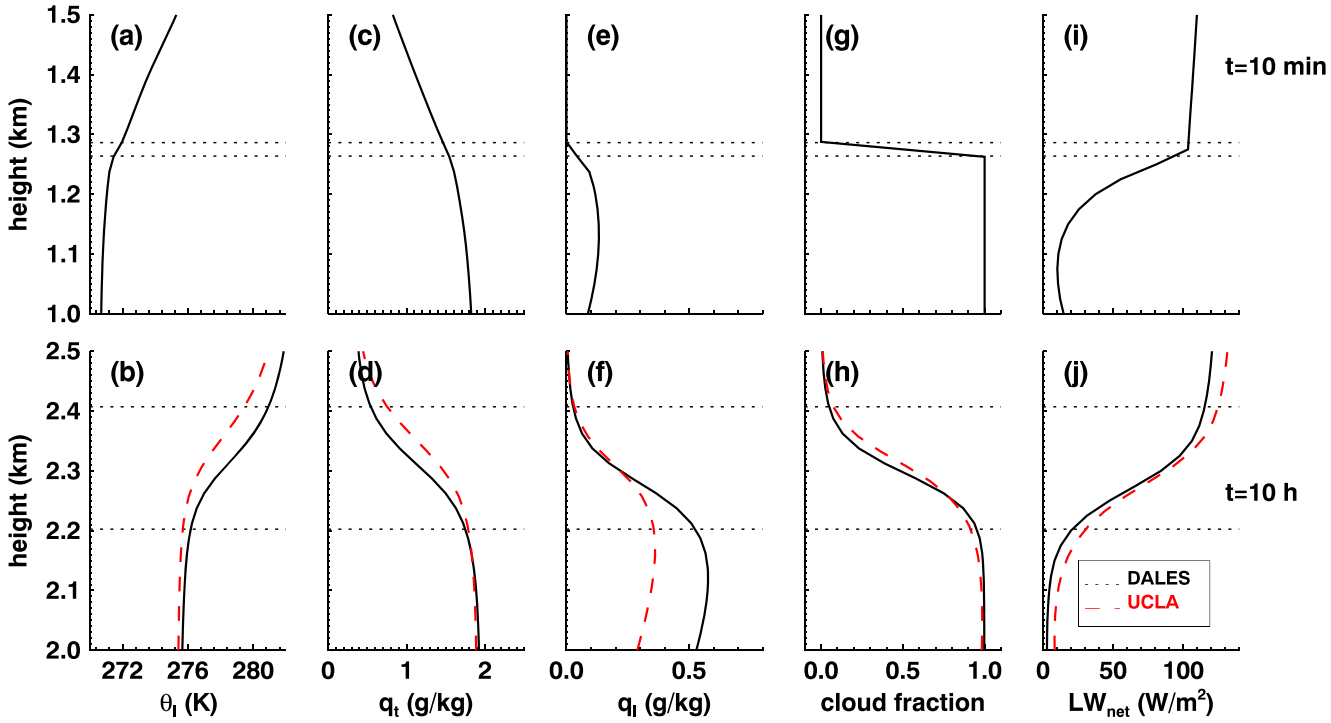

Figure 6. Vertical profiles of horizontal mean profiles of (a, b) θ_l, (c, d) q_t, (e, f) q_l, (g, h) cloud fraction, and the (i, j) net longwave radiative flux. The results were obtained from DALES (solid black) and UCLA-LES (dashed, red line) and represent 10-min-averaged values. Furthermore, to facilitate an easy comparison of the inversion layer structure, the UCLA-LES results were shifted upward by 170 m. The plots in the top row were obtained from the first 10 min of the simulation, and the bottom plots at $t = 10$ hr. The dotted lines indicate the heights where the cloud fraction from DALES crosses arbitrary thresholds of 0.05 and 0.95. For the lower plots this corresponds well with the boundaries of the thermal inversion layer. The model names are given in Table 1.

Figure 6 shows the vertical thermodynamic structure and the net longwave radiative flux profiles near the cloud top and the inversion layer during the stratocumulus dominated phase of the CAO obtained with DALES and UCLA-LES. The upper row depicts the results just after the initialization. The jump of the net longwave radiative flux across the top of the cloud layer is almost 100 W/m^2. This value is significantly larger than for typical subtropical stratocumulus and is predominantly due to the very low specific humidity values and low temperatures aloft. The jump in the net longwave radiative flux takes place across the upper part of the cloud layer but below the base of the inversion layer. This placement implies a strong cooling of the cloud top and is in accord with observations collected in stratocumulus clouds (Duynkerke et al., 1995).

However, the results shown in the bottom row of Figure 6, which were obtained at $t = 10$ hr, give a somewhat different picture. From the vertical profiles of θ_l and q_t it can be seen that the mean inversion layer thickness is about 200 m. Furthermore, the nonzero values for the cloud fraction and cloud liquid water indicate that convective clouds reach the inversion top. Most importantly, a significant fraction of the longwave radiative cooling is found to take place within the inversion layer. Let us perform a thought experiment in which a motionless cloud layer with constant $\theta_{l,\mathrm{cld}}$ is capped by a warm inversion layer. After some time radiation will have cooled the inversion layer air to the cloud layer value. If one determines the depth of the boundary layer by the height above which θ_l starts to deviate from the cloud layer value, the radiatively cooled inversion layer will be diagnosed as boundary layer air. In this case the boundary layer height is found to grow with time on the basis of the vertical θ_l structure, but this growth is obviously not due to entrainment.

The cooling rate of inversion layer air by radiation can be computed from

$$\left(\frac{\partial \theta_l}{\partial t}\right)_{\mathrm{LW\ rad}} = -\frac{1}{\rho c_p \Pi}\frac{\partial F_{\mathrm{LW,net}}}{\partial z}, \tag{10}$$

with Π the Exner function and c_p the specific heat of air at constant pressure. The change of the net longwave radiative flux across a layer with a thickness $\Delta z_{\mathrm{inv}} = 225$ m is about $\Delta F_{\mathrm{LW,net}} = 92$ W/m^2. If we approximate the θ_l profile in the inversion layer as a linear function of height, we can express its mean value as $\theta_{l,\mathrm{cld,top}} +$

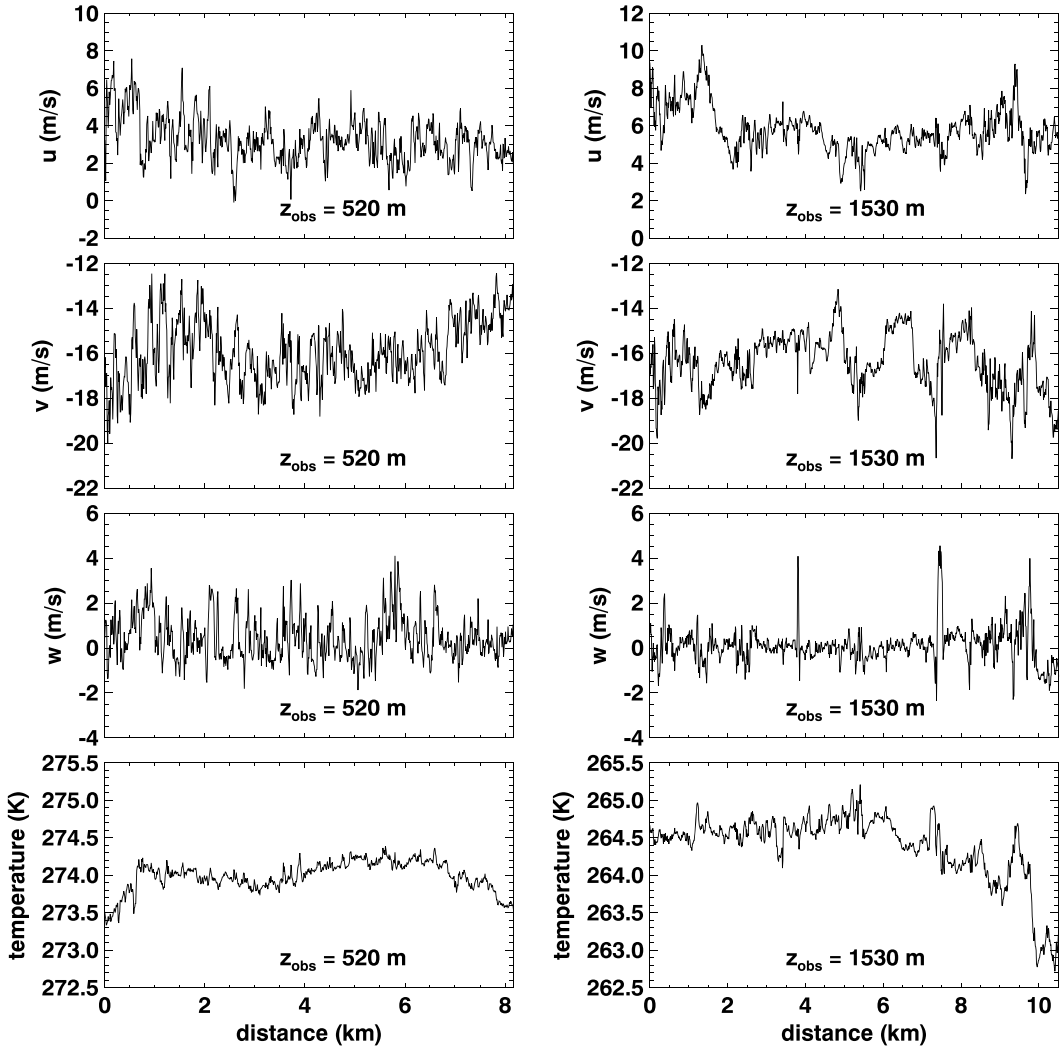

Figure 7. Aircraft observations of the zonal u, meridional v, and vertical w wind components and temperature T in the subcloud and cloud layers, respectively. The observations were collected during a period that corresponds approximately to the last quarter of the simulation time.

$\Delta\theta_l/2$. A cooling of inversion layer down to a value of $\theta_{l,\mathrm{cld,top}}$ gives a radiative time scale of

$$\Delta t_{\mathrm{rad}} = \rho c_{\mathrm{p}} \Pi \frac{\Delta\theta_l}{2} \frac{\Delta z_{\mathrm{inv}}}{\Delta F_{\mathrm{LW,net}}} \approx 4,360\,\mathrm{s}, \tag{11}$$

where we used $\Delta\theta_l = 3.8$ K, $\rho = 1.02$ kg/m^3, and $\Pi = 0.92$. We conclude that during an approximate period of about 1 hr the inversion layer would obtain the same θ_l as the cloud top. If no processes other than radiation were influencing the temperature profile, this time scale may be interpreted as boundary layer growth by direct radiative cooling, at a rate of about 5.2 cm/s. The high values of the boundary layer growth rates, as shown in Figure 4g, are therefore due to both turbulence-driven entrainment, in part by an increasing latent heat release in the cloud layer through enhanced latent heat fluxes, and direct radiative cooling of the inversion layer.

A few short aircraft legs with observations of the wind velocity and temperature are available for times that correspond to the last quarter of the simulation period. Figure 7 shows that in the subcloud layer there is homogeneous turbulence, whereas in the cloud layer a few spikes in the observed vertical velocity indicate the presence of convective cumulus clouds. The fluctuations in both horizontal wind velocity components are rather large, with the difference between their minimum and maximum values being about 8 m/s.

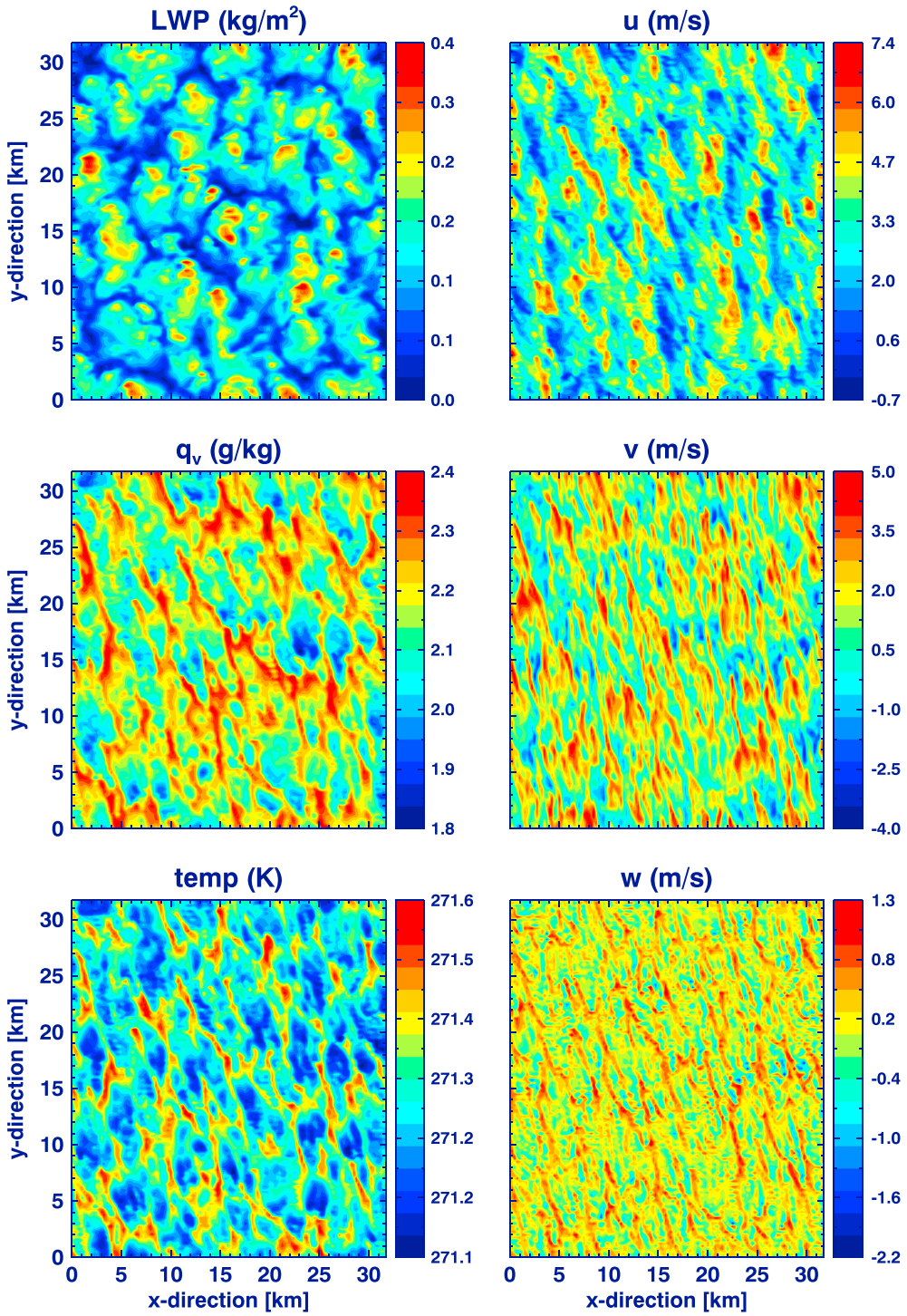

Figure 8. Contour plots of instantaneous fields of liquid water path (LWP) and fluctuations with respect to the horizontal mean values of the three wind components u, v, and w, the water vapor specific humidity q_v, and the temperature T at a height of 100 m after 3-hr simulation time for the reference case as obtained from the UCLA-large eddy simulation model. UCLA-large eddy simulation. To allow the visibility of the structures, only 1/3 of the total horizontal domain size is shown.

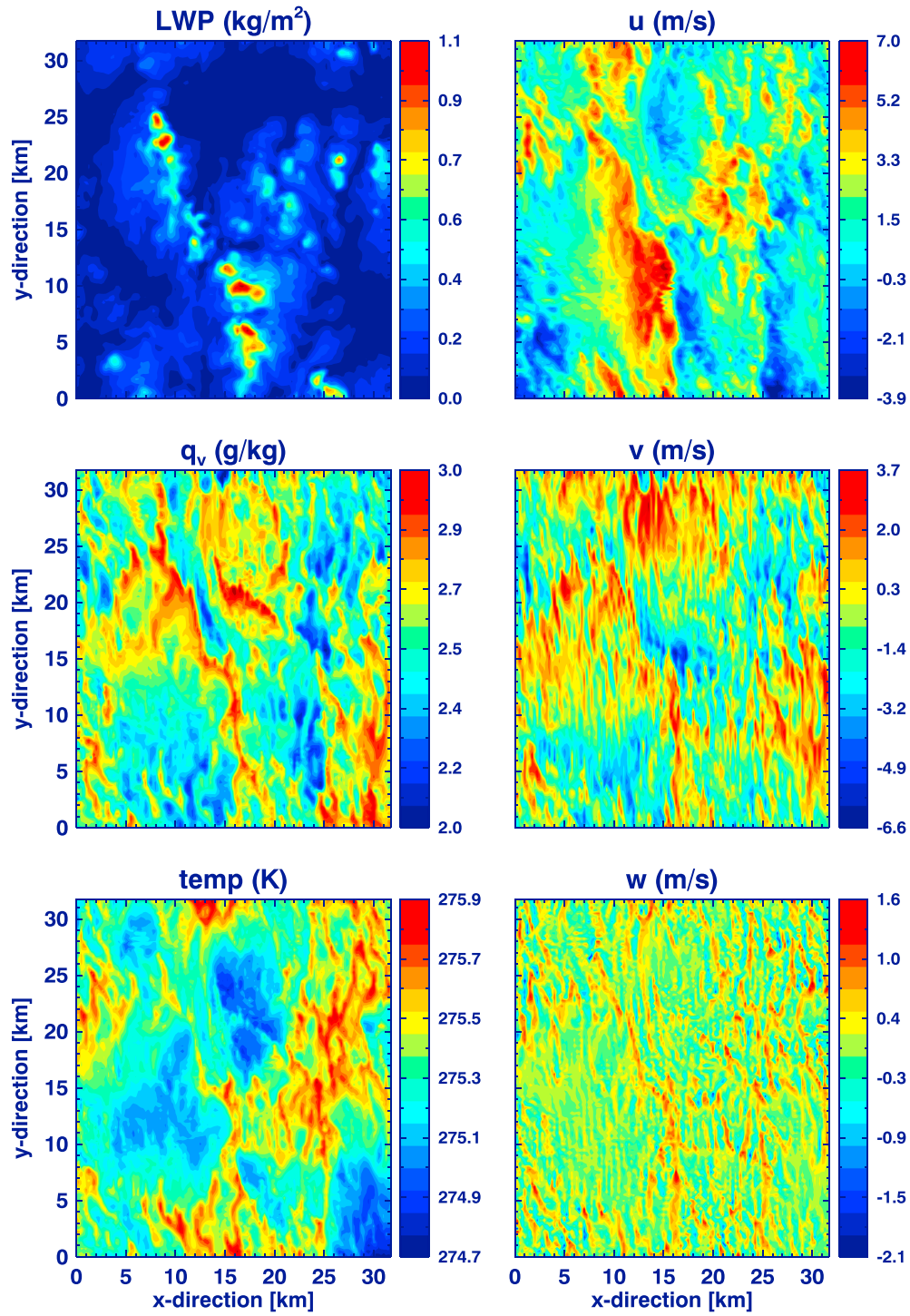

Figure 9. As Figure 8 but at $t = 12$ hr for the reference case as obtained from the UCLA-large eddy simulation model.

High-frequency fluctuations in the observed temperature are small compared to the fluctuations occurring at the kilometer scale, varying from about 1 K in the subcloud layer to about 2 K in the cloud layer.

Figures 8 and 9 show some instantaneous fields from the MPI/UCLA-LES model at $t = 3$ and 12 hr, respectively. The results of the LWP at $t = 3$ hr do not show the organization of cloud streets. However, at a height of 100 m it can be seen that the vertical wind velocity field clearly displays elongated structures of upward motions. Organized horizontal structures with an approximate length of about 10 km are also

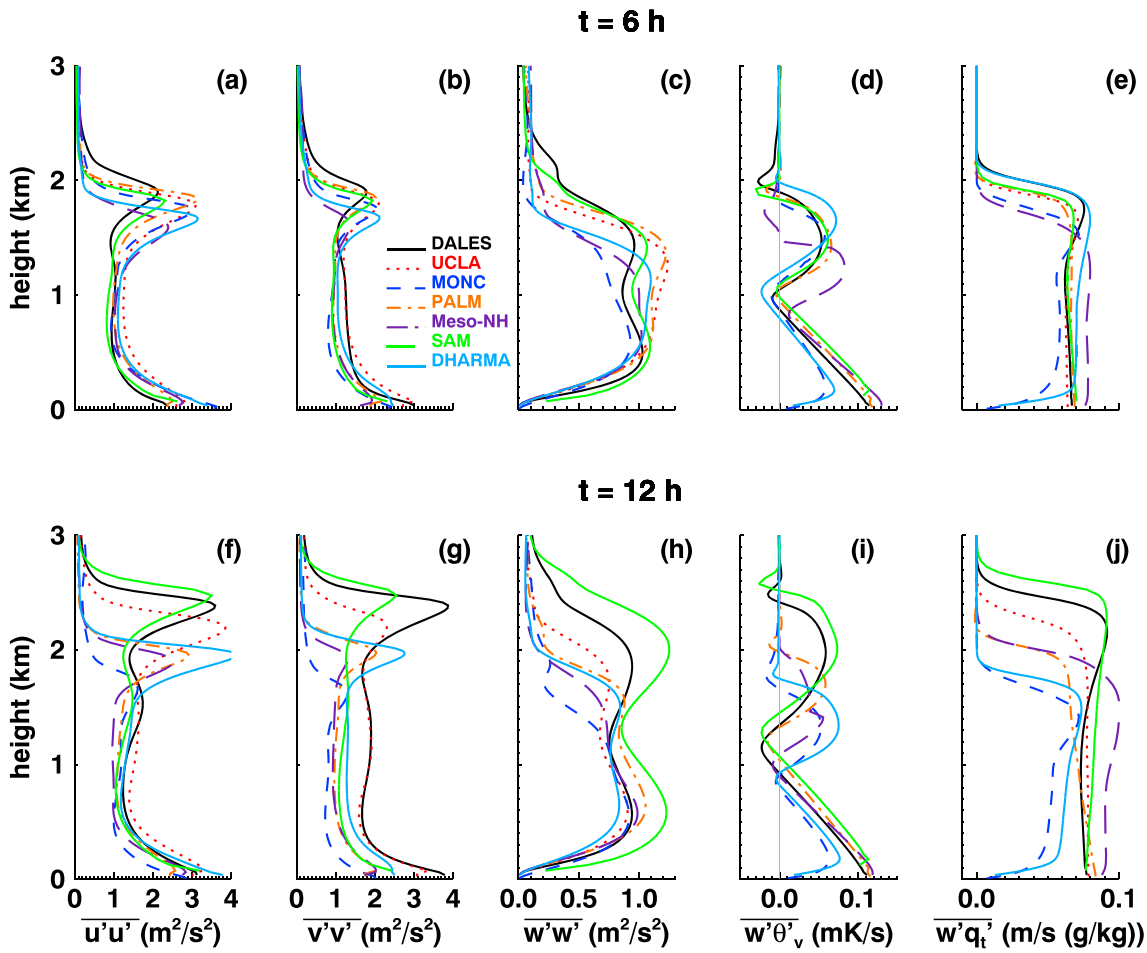

Figure 10. Reference case results at $t = 6$ hr (upper row) and $t = 12$ h (lower row) for the vertical profiles of resolved variances of (a, f) $\overline{u'u'}$, (b, g) $\overline{v'v'}$, (c, h) $\overline{w'w'}$, and total fluxes of (d, i) $\overline{w'\theta_v'}$, (e, j) $\overline{w'q_t'}$. The results represent 10-min mean values as provided by the modelers. For MONC and DHARMA $\overline{w'\theta_v'}$ and $\overline{w'q_t'}$ were not available, and for convenience we plotted their resolved values as diagnosed from the instantaneous 3-D fields for MONC and DHARMA. The line styles are according to the legend. The gray line shown in (d) and (i) indicates the zero axis. The model names are given in Table 1.

evident in the temperature, specific humidity, and horizontal wind velocity components. Note that in the cloud layer the spatial structures in the LWP strongly resemble those of the total water specific humidity and temperature (cf. De Roode & Los, 2008, their Figure 1). Figure 9 shows that at $t = 12$ hr all quantities shown exhibit mesoscale structures. The temperature field shows cold regions that appear to be surrounded by a circular band of rising motions. In the lower right part of the subdomain we find an area of low temperatures and high specific humidity values. These are likely caused by the partial evaporation of precipitation, which cause a cooling and a moistening. At $t = 12$ hr there is no street-like organization in the horizontal wind anymore. However, note that the horizontal wind velocity exhibits large mesoscale fluctations, with both u and v showing variations of almost 10 m/s across a distance of about 10 km. The magnitude of those relatively large horizontal wind velocity fluctuations is in agreement with the aircraft observations.

The ratio of shear to buoyancy production is a key quantity explaining whether convection organizes in rolls or cellular convection (Salesky et al., 2017). Gryschka and Raasch (2005) and Gryschka et al. (2008) have carried out LES of CAOs and investigated the cause for the appearance of free roll convection, which is observed in almost any CAO in satellite picture in terms of cloud streets. They found that for a weak CAO, namely, with $-h/L < 10$, rolls appear by a pure self organization of the flow. Here h is the boundary layer height and L the Monin-Obukhov length:

$$L = -\frac{u_*^3 \theta_v}{\kappa g \overline{w'\theta'_v}_{sfc}}, \tag{12}$$

with $\kappa = 0.4$ the von Karman constant, $u_* = (\overline{u'w'}^2_{sfc} + \overline{v'w'}^2_{sfc})^{1/4}$ the friction velocity, and g the acceleration due to the Earth's gravity. For moderate and strong CAO with $-h/L > 10$ rolls developed only by including the influence of heterogeneities in the ice edge, where roll development was triggered. This situation is not considered in the present study. They called these two types of organized convection "free roll convection" and "forced roll convection," respectively. During the first few hours of the UCLA-LES simulation $L \approx 300$ m, and since $h < 3$ km the critical condition for roll convection is satisfied. The fact that roll structures are present in its near surface vertical velocity field, the reason that no cloud streets are present in the simulations is not fully understood by the authors. As a speculation, it may be possibly due to the relatively high altitude of the stratocumulus cloud deck, where the effects of surface drag on the vertical wind shear are not sufficiently strong. In any case, Gryschka et al. (2014) showed for a wide parameter range of CAOs that even when rolls contribute up to 50% to vertical transports, the total fluxes were not enhanced compared to the same meteorological situation but without rolls.

Figure 10 presents the resolved components of the TKE=$\frac{1}{2}(\overline{u'u'} + \overline{v'v'} + \overline{w'w'})$, in addition to the sum of the resolved and subgrid vertical turbulent fluxes of θ_v and q_t, respectively. The models give qualitatively similar vertical profiles for the horizontal components of the TKE, $\overline{u'u'}$, and $\overline{v'v'}$. However, a close inspection of $\overline{v'v'}$ shows that in the bulk of the boundary layer their values differ by a factor of 2 among the models. The vertical profiles of $\overline{w'w'}$ and $\overline{w'\theta'_v}$ in the subcloud layer are very similar to the ones found in the clear convective boundary layer (cf. De Roode et al., 2016), and the presence of distinct local minimum values for both is indicative of the presence of cumulus clouds. If $\overline{w'\theta'_v} < 0$ it will act as a sink term in the prognostic equation for $\overline{w'w'}$, thereby explaining the local minima of the latter quantity.

In case rising thermals become saturated with water vapor, the latent heat release will increase the buoyancy of the cumuli allowing them to rise further, thereby providing the stratocumulus layer above with moisture (Stevens et al., 1998). Processes like cloud top entrainment of relatively warm and dry inversion air, the formation of precipitation and its subsequent partial evaporation that cools and moistens the subcloud layer, and absorption of solar radiation by the cloud layer are all processes that can lead to a distinct layered structure of the boundary layer. Such a stratification is often referred to as decoupling (Bretherton & Wyant, 1997). Decoupling has been found to lead to a strong reduction of the humidity transport from the subcloud layer to the stratocumulus above, in particular for daytime conditions in subtropical SCTs (De Roode et al., 2016; Sandu et al., 2010; Sandu & Stevens, 2011). Although the negative values of $\overline{w'\theta'_v}$ at the top of the subcloud layer hint at a decoupled boundary layer structure in the CAO studied here, the approximate linear variation of $\overline{w'q'_t}$ with height (see Figures 10e and 10j) indicates an efficient turbulent transport of moisture from the surface to the top of the boundary layer.

4. Scale Dependency of Subgrid and Resolved Fluxes and Variances

Although the horizontal mesh Δx of 250 m is rather coarse for an LES, it is much finer than the mesh size that is typically used in weather forecast and climate models. Following Honnert et al. (2011), we have applied a subdomain decomposition to the LES fields to diagnose how the resolved and subgrid fluxes should be partitioned as a function of an assumed applied mesh size Dx such as used in a large-scale model. Here we have deliberately introduced Dx to stress that the results are diagnosed for such a grid spacing and from LES fields that were performed on a smaller mesh of Δx. Such analyses are key to design scale-aware parameterizations in the gray zone (Boutle et al., 2014; Malavelle et al., 2014). As a next step we investigate what happens if the LESs are run on an even coarser horizontal grid.

4.1. Horizontal Coarsening of Results

The simulations were performed on a horizontal domain consisting of $N_x \times N_y$ grid points with a uniform horizontal mesh of Δx. Let us consider two arbitrary quantities, φ and ψ. The horizontal mean of an arbitrary quantity φ across the domain is indicated by an overbar and is given by

$$\overline{\varphi}(z) = \frac{1}{N_x N_y} \sum_{i=1}^{N_x} \sum_{j=1}^{N_y} \varphi_{ij}(z), \tag{13}$$

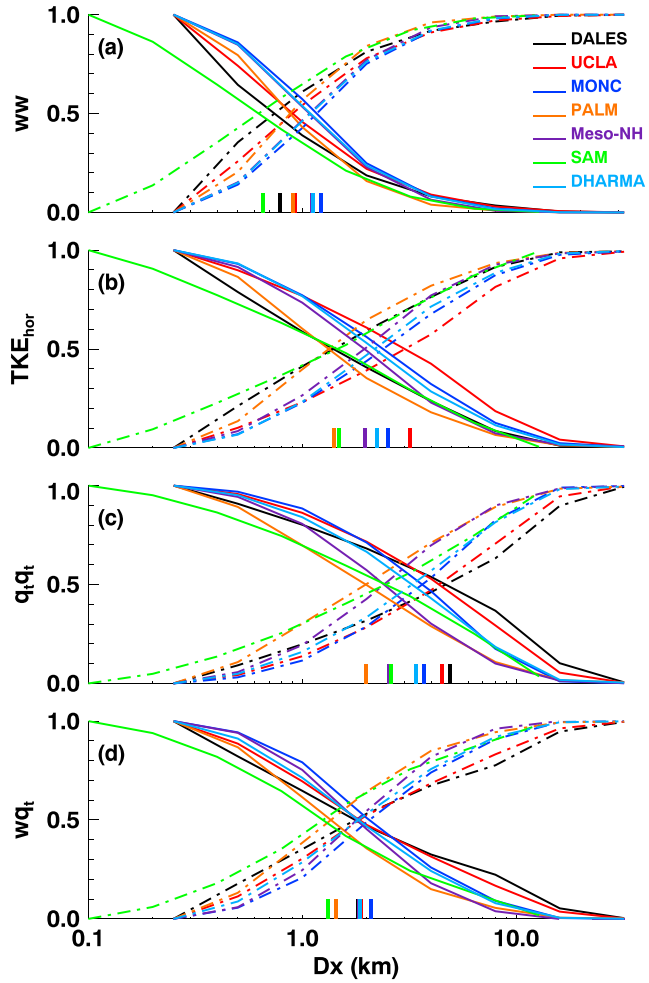

Figure 11. The resolved (solid lines) and subgrid (dash-dotted lines) values for (a) ww, (b) $\mathrm{TKE_{hor}} = 0.5(\overline{u'u'} + \overline{v'v'})$, (c) $q_t q_t$, and (d) wq_t, normalized by their sum, as a function of the coarsening filter Dx according to equations (17) and (18), for the reference case at $t = 12$ hr at a height of 1.5 km. The short vertical lines at the bottom of the plots indicate for each model the critical grid size for which its subgrid and resolved parts are equal. The line styles are according to the legend.The model names are given in Table 1.

and the covariance

$$\overline{\varphi'\psi'} = \frac{1}{N_x N_y} \sum_{i=1}^{N_x} \sum_{j=1}^{N_y} (\varphi_{ij} - \overline{\varphi})(\psi_{ij} - \overline{\psi}). \tag{14}$$

Following Honnert et al. (2011), we decompose the horizontal domain into $M_x \times M_y$ smaller subdomains, where each one contains $n_x \times n_y$ grid points, with $n_x = N_x/M_x$. The mean of φ in a subdomain is expressed with angular brackets:

$$\langle \varphi \rangle_{kl} = \frac{1}{n_x n_y} \sum_{i=1}^{n_x} \sum_{j=1}^{n_y} \varphi_{ij} \tag{15}$$

with $1 \leq k \leq M_x$ and $1 \leq l \leq M_y$ the indices of the subdomain. $\langle \varphi \rangle$ can be interpreted as the resolved value of φ for a horizontal mesh $Dx = n_x \Delta x$. As such Dx may also be interpreted as a coarsening filter size. The subgrid covariance in a subdomain can be determined according to

$$\langle \varphi'' \psi'' \rangle_{kl} = \frac{1}{n_x n_y} \sum_{i=1}^{n_x} \sum_{j=1}^{n_y} (\varphi_{ij} - \langle \varphi \rangle_{kl})(\psi_{ij} - \langle \psi \rangle_{kl}). \tag{16}$$

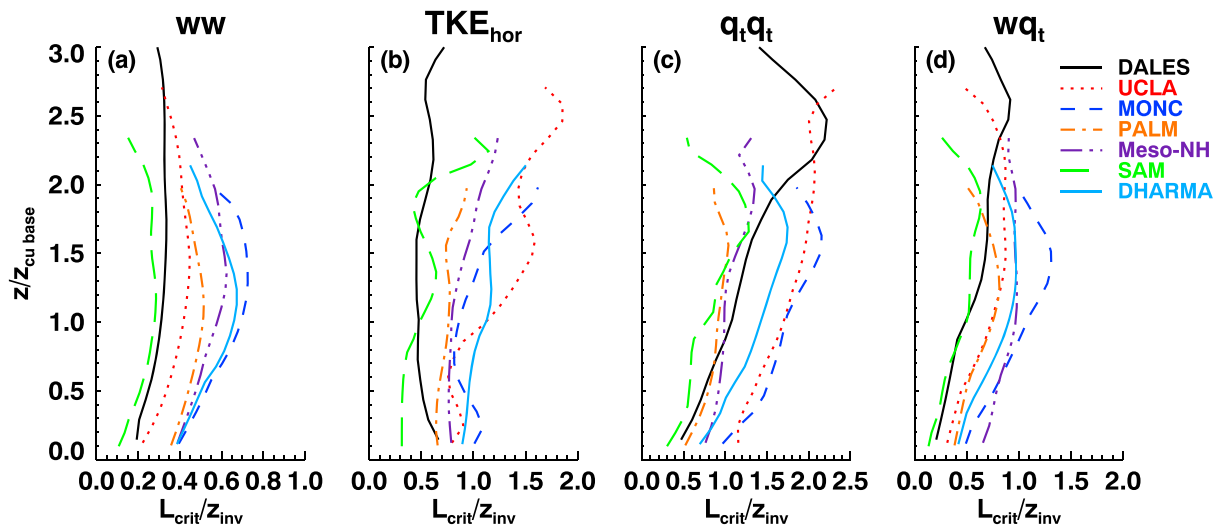

Figure 12. The normalized critical length scale as a function of normalized height at t =12 hr for the variances (a) $\overline{w'w'}$, (b) $\mathrm{TKE_{hor}}$=0.5($\overline{u'u'}+\overline{v'v'}$), (c) $\overline{q_t'q_t'}$, and the (d) vertical flux $\overline{w'q_t'}$. Line styles are according to the legend. The model names are given in Table 1.

Here we recall that double primes are used to indicate that the fluctuations are computed with respect to the local subdomain mean values. We can compute the domain mean resolved covariance from the subdomain mean values according to

$$\overline{\varphi'\psi'}^{\mathrm{res}} = \frac{1}{M_x M_y}\sum_{k=1}^{M_x}\sum_{l=1}^{M_y}(\langle\varphi\rangle_{kl}-\overline{\varphi})(\langle\psi\rangle_{kl}-\overline{\psi}). \tag{17}$$

The domain mean subgrid covariance is given by

$$\overline{\varphi''\psi''}^{\mathrm{sub}} = \frac{1}{M_x M_y}\sum_{k=1}^{M_x}\sum_{l=1}^{M_y}\langle\varphi''\psi''\rangle_{kl}. \tag{18}$$

It can be derived that the sum of the domain mean resolved and subgrid covariances as computed from the subdomain decomposition is equal to the domain mean covariance:

$$\overline{\varphi'\psi'}^{\mathrm{res}} + \overline{\varphi''\psi''}^{\mathrm{sub}} = \overline{\varphi'\psi'}. \tag{19}$$

For $M_x = M_y = 1$, $\overline{\varphi'\psi'}^{\mathrm{res}} = 0$, and $\overline{\varphi''\psi''}^{\mathrm{sub}} = \overline{\varphi'\psi'}$, and if $M_x = N_x$ and $M_y = N_y$, $\overline{\varphi'\psi'}^{\mathrm{res}} = \overline{\varphi'\psi'}$, and $\overline{\varphi''\psi''}^{\mathrm{sub}} = 0$.

The results of the resolved and subgrid values of $\overline{w'w'}$, $\mathrm{TKE_{hor}} = 0.5(\overline{u'u'}+\overline{v'v'})$, $\overline{q_t'q_t'}$, and $\overline{w'q_t'}$, normalized by their respective total values, are displayed as a function of the coarsening filter size Dx at t = 12 hr at a height of 1.5 km in Figure 11. The effect of mesoscale structures is clearly visible in the sense that up to scales of 10-km resolved fluctuations contribute to the variances and fluxes. Honnert et al. (2011) were the first to analyze the scale dependency of the flux partitioning for the clear convective boundary layer and one with shallow cumulus clouds. In agreement with their study we find that the partitioning depends on the specific quantity considered, with larger values for the resolved variances of $\overline{u'u'}+\overline{v'v'}$ and $\overline{q_t'q_t'}$ as compared to $\overline{w'w'}$.

Following Honnert et al. (2011), we define the critical length scale L_{crit} as the length where the subgrid and resolved fluxes have the same magnitude. The critical length scales for $\overline{w'q_t'}$ are in between the values found for the variances of $\overline{w'w'}$ and $\overline{q_t'q_t'}$, respectively. The SAM results, which were obtained with a horizontal mesh of 100 m, indicate that the contribution of resolved motions on the vertical transports at length scales between 100 and than 250 m are not negligibly small. Its values are somewhat smaller but close to the values that were obtained from DALES (see Figure 12).

We also performed a similar scaling for L_{crit} as Honnert et al. (2011), using the boundary layer depth, z_{inv}, and the depth of the subcloud layer as determined from the lowest heights where cumulus clouds are present,

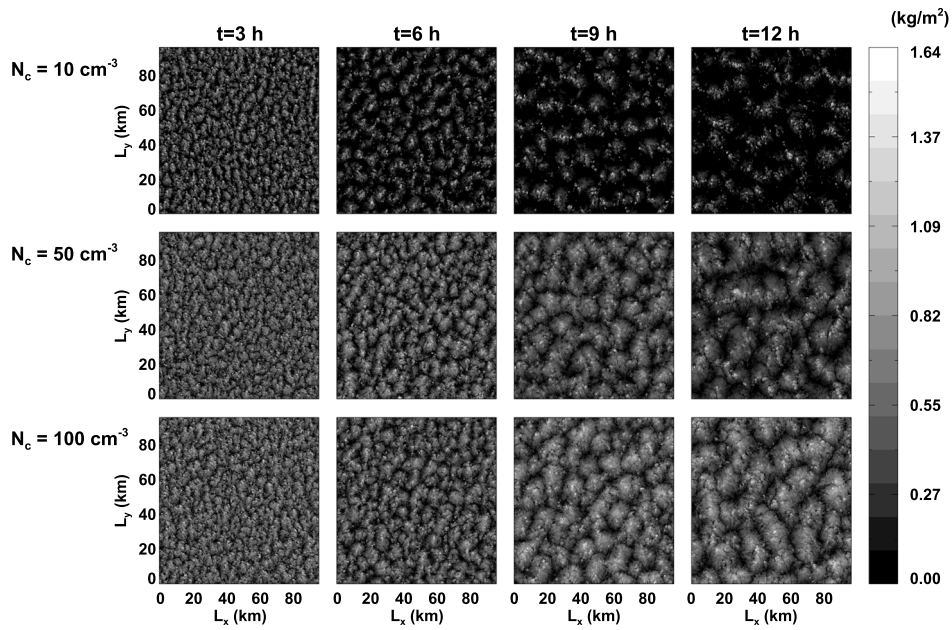

Figure 13. Dutch Atmospheric large eddy simulation liquid water path fields for three different droplet concentrations, $N_c = 10$, 50, and 100 cm^{-3} (top, middle, and bottom rows, respectively) at four different times ($t = 3$, 6, 9, and 12 hr, as indicated above the respective columns). For $N_c = 50$ and 100 cm^{-3} the cloud cover is equal to unity at any time but reduces to 0.64 at $t = 12$ hr for $N_c = 10$ cm^{-3}.

$z_{cu,base}$. The largest values for the critical length scales for any of the quantities shown in Figure 12 are found in the cloud layer. Furthermore, the values for L_{crit} depend on the quantity considered and are smallest for the vertical velocity and largest for moisture. This was also found from fields of shallow cumulus clouds studied by Honnert et al. (2011), although a comparison shows that for their case the typical values for L_{crit} are smaller than for the CAO case considered in this study. The development of humidity fluctuations at the mesoscales have been found in nonprecipitating stratocumulus but also in the dry convective boundary layer (De Roode et al., 2004). The growth of mesoscale fluctuations of any quantity appears to be tightly connected to the production of variance (De Roode et al., 2004). The budget equation for the variance of q_t is given by

$$\frac{\partial \overline{q_t'^2}}{\partial t} = -2\overline{w'q_t'}\frac{\partial \bar{q}_t}{\partial z} - \frac{\partial \overline{w'q_t'q_t'}}{\partial z} - \epsilon_{\overline{q_t'^2}} + \overline{S'_{q_t}q_t'}, \tag{20}$$

where the first three terms on the right-hand side indicate the production, transport, and dissipation of variance, respectively. The last term represents the effect of a local, nonadiabatic source, such as the evaporation of drizzle. In the absence of such a source term the mean variance will only grow if its production exceeds the net effect of dissipation and transport. We observe from Figure 12 that the critical length scales from SAM and DALES are rather small as compared to the other models. These two models maintained a solid stratocumulus cloud deck and produced relatively little precipitation. More drizzle, as found from the other models, may promote larger values for the critical length scales by its potential to produce moisture variance through the last term in equation (20) and also from its capability to enhance the variance production term by steepening the mean vertical gradient of q_t through the removal of cloud water from the cloud layer and the subsequent moistening of the subcloud layer by its partial evaporation (cf. Zhou et al., 2018). This will result in buoyancy fluctuations, which, in turn, will impact the vertical velocity.

5. Microphysics Sensitivity Experiments

Here we investigate some sensitivity experiments performed with different prescribed values for N_c, as well as runs including ice microphysics. Using satellite retrievals, Field et al. (2017) suggest a decrease in N_c from about 50–100 cm^{-3} in the stratocumulus deck to only 10 cm^{-3} in the cumulus dominated regime at the end of the trajectory. This trend suggests a removal of boundary layer accumulation mode aerosols via precipitation processes, similar to what has been reported in recent observational studies (Abel et al., 2017)

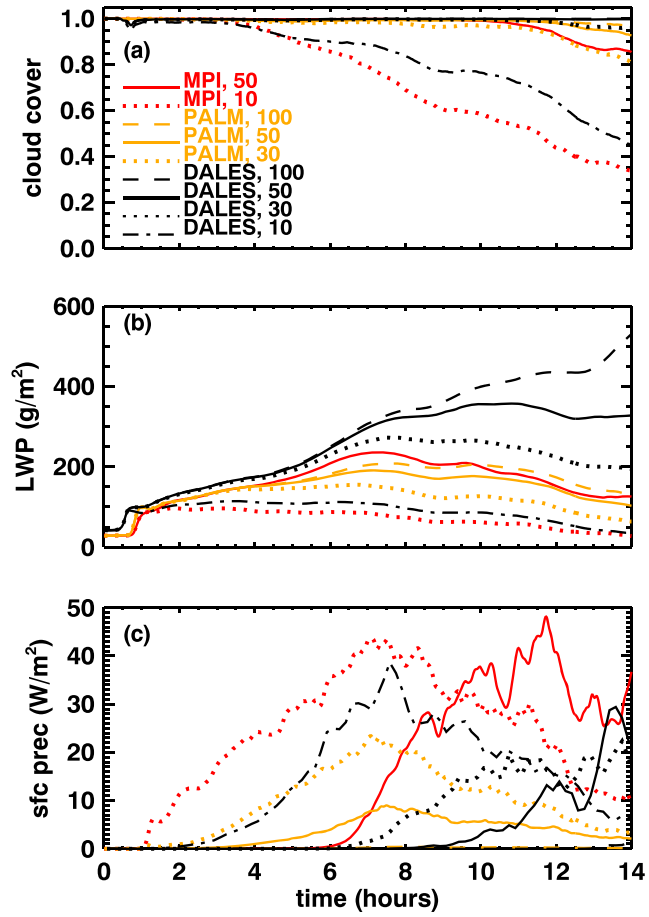

Figure 14. Time series of (a) cloud cover, (b) LWP, and (c) surface precipitation for different cloud droplet number concentrations (cm^{-3}) as obtained from UCLA-LES, PALM, and DALES. Line styles are according to the legend. The model names are given in Table 1. LWP = liquid water path.

and modeling results (Yamaguchi et al., 2017). Because only a few LES models have the capability to include this process, all simulations presented here use constant values for N_c.

5.1. Effect of Changing the Cloud Droplet Number Concentration

To address the sensitivity of the cloud evolution to the prescribed N_c value, some additional simulations were performed with values for N_c in the range of observed values between 10 and 100 cm^{-3}. The resulting changes in the cloud effective radius and the cloud optical depth were computed from the mean volume radius of the droplets and the assumption of lognormal cloud droplet size distribution following Van der Dussen et al. (2013). The contour plots for the LWP as obtained from DALES are shown in Figure 13. For any of the values for N_c we find a gradual growth of the cloud cell sizes with time. One of the main differences between the simulations is that the cloud cover remains equal to unity, except for the one with $N_c = 10$ cm^{-3} that gives open cells, with a cloud cover of 0.64 after 12-hr simulation time. This resulting formation of open cells for reduced cloud droplet number concentrations is similar to what has been found from LES of subtropical stratocumulus clouds (Wang & Feingold, 2009). Figure 14 illustrates how a reduction of N_c generally leads to an earlier timing of the breakup of the cloud layer, smaller LWP values. and enhanced values of surface precipitation. These effects are, first of all, due to the fact that a reduction of N_c yields larger droplet sizes which tend to enhance the formation of precipitation, which allows for a more efficient removal of moisture from the cloud layer (Albrecht, 1989). Similar sensitivity runs were also performed with DALES using the microphysics scheme of M. F. Khairoutdinov and Kogan (1999), but in these simulations the reductions in cloud amount were less strong as compared to results obtained with the Seifert and Beheng (2006) scheme.

The value of N_c also has an indirect effect on cloud top entrainment. At the top of the cloud layer evaporation of cloud droplets takes place by entrainment and subsequent mixing of relatively warm and dry air from

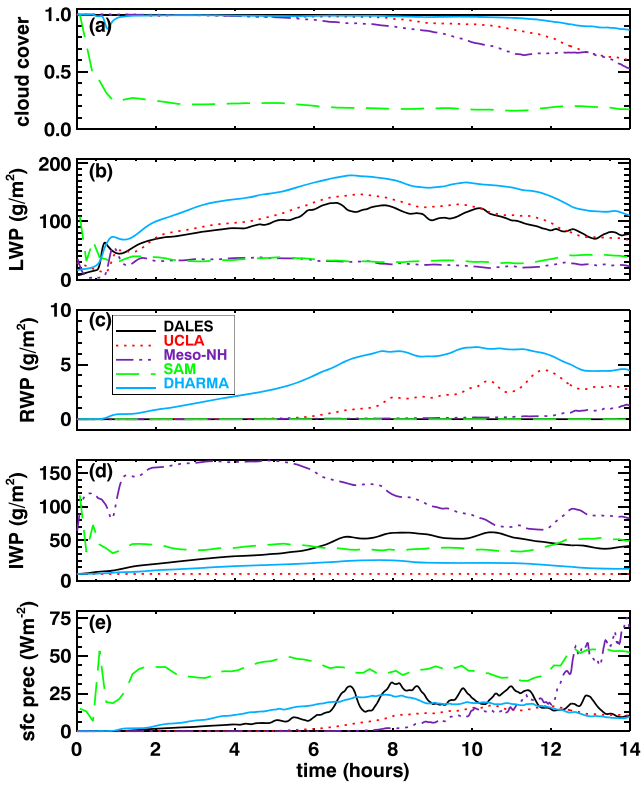

Figure 15. Time series for the ice microphysics case of (a) the cloud cover, (b) the cloud liquid water path, (c) the rain water path, (d) the total ice water path, and (e) the precipitation flux at the surface. The line styles are according to the legend. LWP = liquid water path; RWP = rain water path; IWP = ice water path; The model names are given in Table 1.

just above the inversion. The strength of the evaporative cooling will be diminished if less cloud water is available at cloud top to evaporate. This reduction in cloud water results from faster sedimentation of larger droplets at smaller N_c. A smaller evaporative cooling rate will yield a weaker production of buoyancy-driven turbulence and subsequently a decrease of cloud top entrainment (Bretherton et al., 2007). This interaction between microphysics, turbulence, and entrainment, as well as changes in surface heat fluxes, can lead to either an increase or a decrease of the stratocumulus LWP as droplet concentrations decrease (Ackerman et al., 2004; Sandu et al., 2008).

5.2. Ice Microphysics

Figure 15 shows the results from models that include mixed-phase microphysics parameterization. Here the total ice water path (IWP) defines all the contributions from frozen water including ice crystals, snow, graupel, and hail. Unlike the mixed-phase stratocumulus intercomparison study of Ovchinnikov et al. (2014) in which the ice properties (including the number and conditions for ice formation), the processes to omit (namely, aggregation), and the relationships between ice particle maximum dimension, mass, capacitance, and fall speed were all specified for the achieved purpose of reducing model spread, here no such specifications were provided, and thus, the spread of model results is very substantial, reminiscent of earlier intercomparisons such as Klein et al. (2009), with IWP and LWP results each scattering across 2 orders of magnitude. For each model the cloud cover decreases when the ice phase is permitted. However, the partitioning between ice and liquid water differs substantially between the models. In Meso-NH the cloud layer is predominantly in the ice phase. The IWP results in this model are the closest to the estimates in the range of 200–300 g/m^2 reported by Field et al. (2017). The cloud cover in SAM appears to be very sensitive to the inclusion of ice microphysics in the sense that its cloud cover strongly decreases during the spin-up period, which is likely due to the large precipitation flux it generates. The initial strong reduction of the cloud cover strongly diminishes the longwave radiative cooling near the top of the cloud layer needed to sustain the stratocumulus cloud deck. In DALES cloud ice appears in all the columns, although in relatively low con-

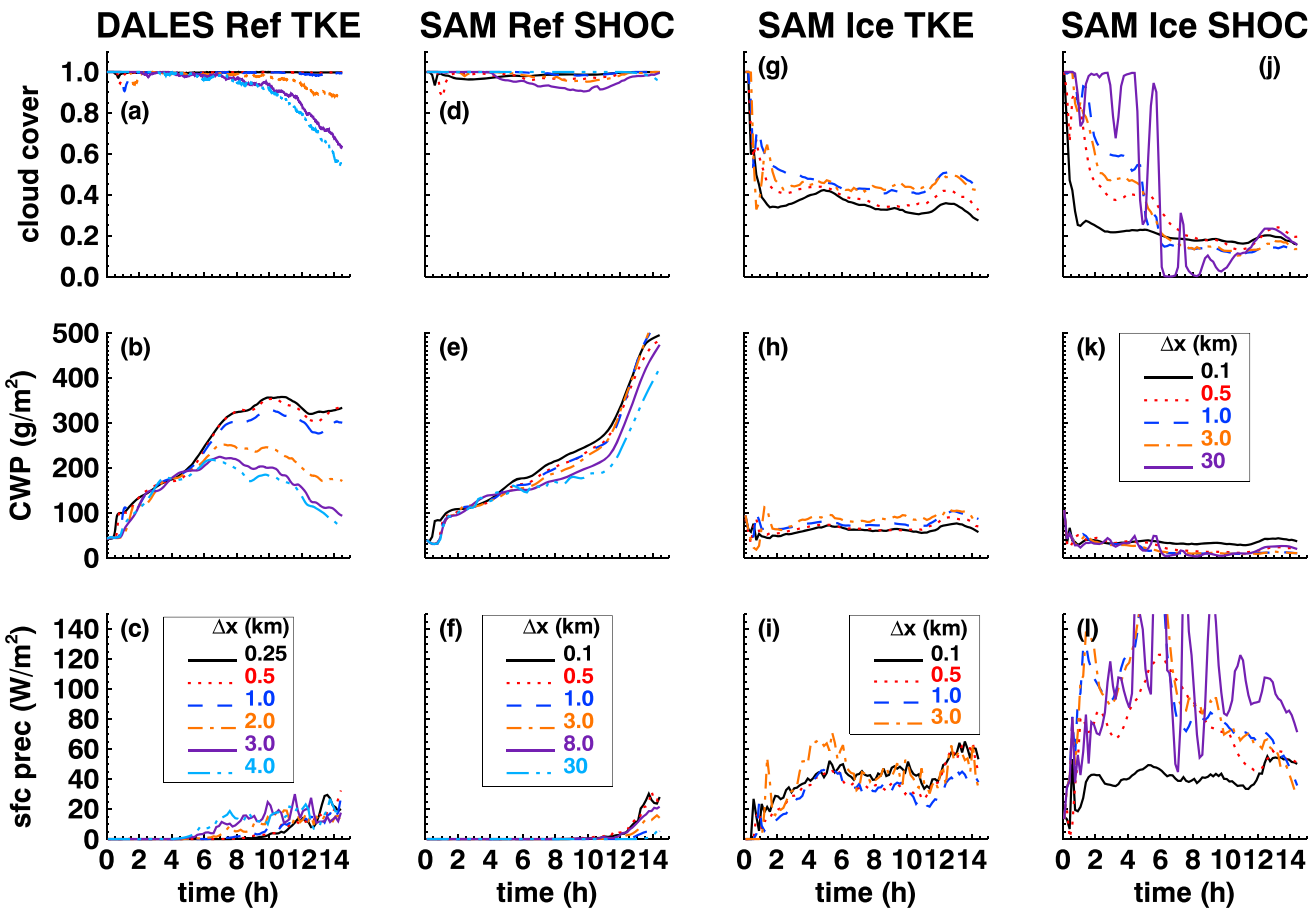

Figure 16. Time series of the cloud cover (a, d, g, and j), total cloud water path (b, e, h, and k), and surface precipitation (c, f, i, and l) for different horizontal grid spacings as obtained for the reference case with DALES (DALES Ref TKE), and SAM using the Simplified Higher-Order Closure (SAM Ref SHOC) as a subgrid model. The two columns on the right show SAM results for the ice case with its TKE (SAM Ice TKE) and SHOC (SAM Ice SHOC) subgrid models, respectively. For easy comparison the axis range of surface precipitation is set to 150 W/m^2. The maximum values for the SAM Ice SHOC results are beyond this range as their values are about 200 W/m^2 for the runs with $\Delta x = 1$ and 3 km, and almost 300 W/m^2 for the run with $\Delta x = 30$ km. The line styles are according to the legends. TKE = turbulent kinetic energy; CWP = cloud water path.

centration. No significant changes in the critical length scales L_{crit} with respect to the reference case results are found if ice is included in the simulations.

A suite of sensitivity runs were carried out with UCLA-LES. In its cloud microphysics scheme the mass m of an ice particle is related to its maximum diameter D through (Seifert & Beheng, 2006)

$$D = a \cdot m^b, \tag{21}$$

with default values $a = 0.217$ and $b = 0.302115$. Test runs with modified values for a and b within the range of observed values (Heymsfield & Iaquinta, 2000; Heymsfield & Kajikawa, 1987) give differences in the LWP and IWP that exceed 1 order of magnitude. Additional runs show that in any case the amount of cloud ice that the model is able to generate seems to be limited. Even with very substantial values for the ice particle number concentration N_{i}, the cloud ice production in this model is modest in contrast to other studies of mixed-phase clouds (e.g., Ovchinnikov et al., 2014). This is most likely a characteristic of the used ice microphysics parameterization. By switching off various processes in the parameterization step-by-step, it was found that the main reason for cloud ice depletion is snow formation through the self-aggregation of cloud ice, a process that was specifically omitted in the Ovchinnikov et al. (2014) intercomparison. Therefore, although the limitation on cloud ice abundance might be a particularity of the specific ice microphysics scheme, the fact that snow, and more generally precipitation, is an important control on cloud condensate amount may constitute a more fundamental feature of the CAO case.

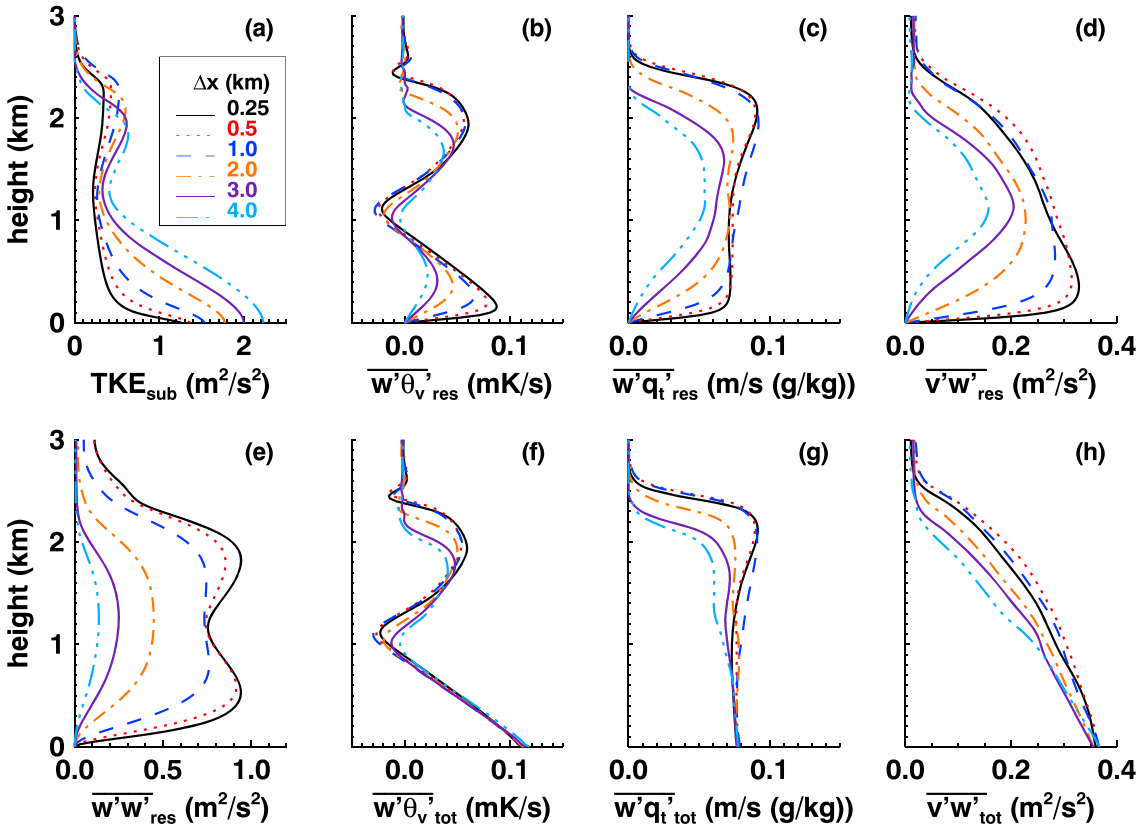

Figure 17. Reference case results of horizontal mean values of (a) the subgrid TKE, the resolved vertical fluxes of (b) θ_v, (c) q_t, and (d) v, (e) the resolved vertical wind variance $\overline{w'w'}$, and the total vertical turbulent fluxes of (f) θ_v, (g) q_t, (h) and v at $t = 12$ hr. The results represent 10-min-averaged values obtained from DALES with different meshes Δx of 0.25, 0.5, 1, 2, 3, and 4 km. The line styles are according to the legend. TKE = turbulent kinetic energy.

6. Running LES in a Numerical Weather Prediction Mode

We have seen how the subgrid contributions to the various fluxes and variances increase with coarsening horizontal mesh size. To take such a dependency into account, Larson et al. (2012) and Boutle et al. (2014) proposed a mesh size-dependent length scale for models that operate at gray zone resolutions. Because the subgrid parameterizations applied in LES models involve a similar dependency on the mesh size, it is tempting to investigate the sensitivity of the results to the horizontal grid spacing. DALES was used for additional simulations of the reference case using the same domain size but in an "eddy-permitting" setting with horizontal meshes of $\Delta x = 0.5$, 1, 2, 3, and 4 km, respectively. The reference case was also run with SAM with its TKE subgrid model replaced by the SHOC scheme for subgrid-scale fluxes and variances (Bogenschutz & Krueger, 2013). SHOC is specifically designed for coarse grid cloud resolving models to better represent turbulence and shallow convective processes including shallow cumulus clouds and the SCT. In addition, SAM also ran the ice case with both the TKE and SHOC subgrid models. For the runs with SHOC applying a horizontal grid spacing of 8 and 30 km the horizontal domain sizes were enlarged to 256^2 and 960^2 km^2, respectively.

The time series of the cloud cover, the total cloud water path, defined as the sum of the LWP and the total IWP, and the surface precipitation are shown in Figure 16. Note that for the reference case clouds are assumed to be free of ice so for this case the cloud water path is identical to the LWP. Up to about 6-hr simulation time, the results from DALES are hardly affected by the choice of the mesh size, even if an unusually large horizontal mesh of 4 km is applied. However, after this period it is found that a coarser horizontal grid spacing leads to an earlier timing of precipitation reaching the surface, causing reductions in both cloud cover and LWP as compared to the high-resolution results.

In contrast to the reference case, which gives overcast stratocumulus for both DALES and SAM, the ice case results for SAM are dominated by broken clouds. A coarsening of the horizontal mesh, from a value for Δx

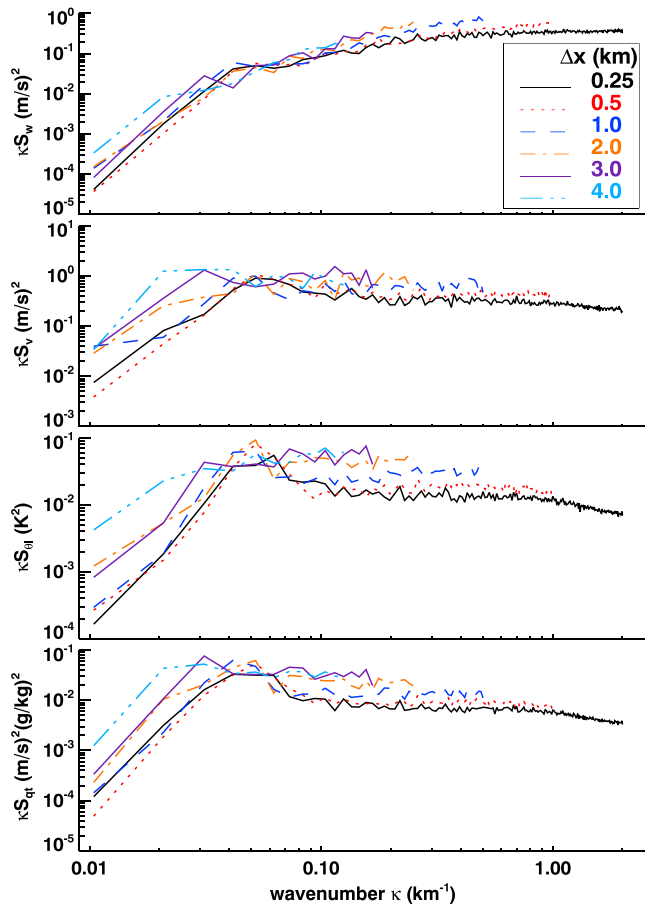

Figure 18. Energy spectra at a height of 1.5 km at $t = 12$ hr for w, v, θ_l, and q_t from DALES reference case runs using horizontal meshes of $\Delta x = 0.25$, 0.5, 1, 2, 3, and 4 km.

of 0.1 km to 0.5, 1, and 3 km, respectively, shows that for SAM the changes in the cloud layer evolution and surface precipitation are rather small for the case with ice (Figures 16g–16i). Another suite of runs with SAM using the SHOC subgrid model shows remarkably robust results for the reference case up to a horizontal grid spacing of 30 km. However, the results for the ice case show much more variation, where a coarsening of the horizontal mesh tends to produce more, and more highly variable precipitation.

Figure 17 shows the sensitivity of the resolved and total vertical fluxes to the horizontal mesh used in DALES. In particular in the subcloud layer the total turbulent vertical fluxes of $\overline{w'\theta_v'}$, $\overline{w'q_t'}$, and $\overline{v'w'}$ appear to be hardly affected by a coarsening of the horizontal mesh. This indicates that a decrease in the resolved vertical turbulent fluxes associated with a coarsening of the horizontal mesh, as shown in Figures 17b–17d, are almost fully compensated by opposite changes in the subgrid fluxes. The parameterization of the subgrid fluxes according to (2), and with the eddy diffusivity according to (4), produces subgrid fluxes whose magnitudes are proportional to $\lambda\tilde{e}^{1/2}$. DALES used a length scale that increases with increasing horizontal grid spacing, $\lambda = (\Delta x \Delta y \Delta z)^{1/3}$. The sensitivity of the subgrid TKE to the grid spacing, as evident in Figure 17a, can be understood from its analytical steady state solution. For the Smagorinsky subgrid TKE equation including buoyancy production both the subgrid TKE and the eddy diffusivity depend on λ^2, which holds even if the stability-dependent length scale according to (8) is used (De Roode et al., 2017). These results indicate some desired scale-aware properties of the TKE subgrid model in the sense that for this particular CAO case the subgrid contribution to the total fluxes compensate smoothly for the loss of resolved fluxes at coarser horizontal mesh sizes.

However, some notable differences arise if the horizontal grid spacing is coarsened, such as the decreasing LWP, but as can be seen from the heights above which turbulence vanishes, the depth of the boundary layer is also affected. To explore to which extent the simulated fields are affected by the horizontal grid spacing, the

energy spectra for momentum (v and w), liquid potential temperature θ_l, and moisture q_t were computed. Figure 18 shows that for coarser horizontal grid spacings the spectral energy of these quantities tends to increase at smaller wavenumbers. Larson et al. (2012) applied SAM to explore its representation of shallow cumulus clouds at horizontal grid spacings up to 4 km. They noted that the resolved vertical velocity variance tends to diminish with coarsening mesh size but that variances of scalars like humidity become too large. They argued that this situation is unwarranted partly because fluctuations in the thermodynamic variables control the microphysics such as drizzle formation. The larger spectral energy for moisture at the smaller wavenumbers, and the larger production of precipitation obtained with DALES for coarsening grid size, is another example that corroborates the findings of Larson et al. (2012). Therefore, the fact that the TKE subgrid scheme exhibits some desired scale-aware properties in terms of its representation of the vertical transport at coarse horizontal grid spacings, this comes with a penalty in terms of a too strong growth of scalar fluctuations at the mesoscales.

7. Conclusions

A CAO case was simulated with seven different LES models. Satellite images and aircraft observations collected in the last part of the trajectory on which the case is based show a gradual transition from overcast stratocumulus off the coast of Greenland to a boundary layer dominated by shallow cumulus clouds north of the United Kingdom. The present work is accompanying two recent studies by Tomassini et al. (2017) and Field et al. (2017) who explored the representation of the CAO case in simulations performed with global and LAMs that operated at gray zone resolutions, with which is meant that the horizontal grid spacing is potentially fine enough (<10 km) to resolve some fraction of the convective transport. LES models are designed to resolve turbulence, and in the present study they were employed to study the temporal evolution of the CAO in addition to its sensitivity to cloud microphysics in terms of prescribed cloud droplet number concentrations and ice microphysics. The following gray zone related issues were elaborated. The length scales of the convective transports were analyzed from the three-dimensional LES fields. Also, the performance of both TKE and higher-order closure subgrid models was tested for horizontal grid spacings (>1 km) that are typically applied by high-resolution weather forecasts.

7.1. General Features of the CAO Case

The LES results for the reference case, which assumed a supercooled liquid cloud, broadly agree in terms of the evolution of a rising stratocumulus cloud deck with the formation of shallow cumulus clouds underneath. This picture is qualitatively similar to what has been found in subtropical stratocumulus to cumulus transitions (SCTs). However, there are a few striking differences with the subtropical SCT. In the CAO case the SHF is about an order of magnitude larger than in the subtropical stratocumulus regime. Also, despite the strong large-scale subsidence that is present in the CAO, the boundary layer depth increases much faster with time in the CAO, with growth rates exceeding 4 cm/s. Also, the very small free tropospheric specific humidity values, and cold free troposphere, both being conditions that are typically present at high latitudes, cause a somewhat stronger longwave radiative cooling than in SCTs. A detailed inspection of results from DALES and UCLA-LES indicates that a significant amount of this radiative cooling takes place within the inversion layer thereby promoting the rapid growth of the boundary layer depth.

The LES models tend to disagree about the timing of the stratocumulus breakup, and some models never exhibit breakup over the 14.5-hr simulation time. The maintenance of the stratocumulus deck is promoted by the strong longwave radiative cooling for this situation, while vice versa, its breakup strongly diminishes the longwave cooling, serving as a positive feedback (cf. Stevens et al., 2005). The breakup of the stratocumulus cloud deck is enhanced for lower values of the prescribed cloud droplet number concentration in the models that considered this variant, or by involving mixed-phase microphysics, where for both processes the removal of cloud water by precipitation processes play a key role. This lack of consistency in the transition of closed to open cells clouds under conditions of freezing temperatures reflects our insufficient understanding of the microphysical processes taking place in this regime. Furthermore, a process that is not captured by the LES models used in this study is the decrease of cloud droplet number concentration through depletion of aerosols by drizzle production, which Yamaguchi et al. (2017) show to accelerate the transition to open cells. These issues urge the need for more direct observations, for example, following a Lagrangian trajectory of an air mass as proposed by Pithan et al. (2018).

7.2. Diagnosis of the Length Scales of Vertical Turbulent Transport

Following Honnert et al. (2011) three-dimensional fields from each of the LES models were used to diagnose the partitioning of subgrid and resolved fluxes and variances as a function of the assumed horizontal mesh, scaling up to sizes more typical of a regional-scale model. The results for the CAO case are in a qualitative agreement with those obtained for the convective boundary layer and shallow cumulus, in the sense that contributions to the vertical velocity variances are dominated by smaller length scales than for other quantities like the specific humidity and the horizontal wind velocity. The analysis of the CAO fields shows that vertical transport of moisture and momentum takes place at horizontal length scales up to about 10 km, which values are typically larger than found for a field of shallow cumulus clouds reported by Honnert et al. (2011). This case therefore demonstrates that for NWPs that use horizontal grid spacings smaller than about 10-km scale-aware parameterizations are necessary for boundary layer regimes like the stratocumulus to cumulus transition.

7.3. What Can We Learn From the LES Results at Gray Zone Resolutions?

The results with coarsened horizontal meshes demonstrate some important scale-aware aspects of TKE subgrid models and the mesh size-dependent length scales used by LES models. It is found that resolved fluxes and variances smoothly diminish with coarsening horizontal mesh. Despite this fact, the total vertical turbulent fluxes appear to be rather insensitive to the horizontal mesh, even if it has a size of 4 km. This finding suggests that operating at gray zone resolutions, models may use a turbulent length scale that depends on the horizontal mesh size. In fact, both Larson et al. (2012) and Boutle et al. (2014) (their equations (1) and (2), respectively) proposed a length scale that depends only on the horizontal mesh size, unlike LES models that generally use a length scale that depends on both the horizontal and vertical mesh sizes. However, at coarse horizontal grid spacings, fluctuations of scalars were found to grow slightly faster at the mesoscales thereby impacting processes like rain formation. The study by Larson et al. (2012) suggested that simulations on a coarse horizontal grid spacing may benefit from a higher-order closure subgrid model. Tests performed with SAM including the SHOC subgrid model showed that even up to a horizontal grid spacing of 30 km its results for the reference case only weakly deviated from the high-resolution run.

Appendix A: Impact of the Spin-Up on the Horizontal Winds in Two Models

Figure A1a shows that after about 1 hr the sign of the tendencies of the east-west wind velocity component u as obtained from DALES and UCLA-LES starts to differ. The results from the other LES models are similar to those found from DALES. After 3 hr the difference in u is about 4 m/s. This difference can be explained by considering the momentum budget equations, which read

$$\frac{\partial \bar{u}}{\partial t} = f(\bar{v} - v_{\mathrm{geo}}) - \frac{\partial \overline{u'w'}}{\partial z}, \tag{A1}$$

$$\frac{\partial \bar{v}}{\partial t} = -f(\bar{u} - u_{\mathrm{geo}}) - \frac{\partial \overline{v'w'}}{\partial z}, \tag{A2}$$

where we neglect large-scale subsidence and we use the fact that no large-scale horizontal advection of momentum is prescribed for the CONSTRAIN case.

The CAO case is initialized with a wind profile, which is not in a geostrophic equilibrium. In general, such a situation will give rise to a harmonic oscillation of the wind velocity (Schröter et al., 2013). Figure A1b shows that after about 1-hr simulation time for DALES, $\bar{v} - v_{\mathrm{geo}} < 0$, whereas in UCLA-LES, $\bar{v} - v_{\mathrm{geo}} > 0$. These differences cause opposing tendencies in u. Figure A1c shows that the rapid change in v after about 40 min observed in UCLA-LES is due to its strongly fluctuating momentum flux $\overline{v'w'}$. Such variations are associated with the spin-up phase, typically lasting about 2 hr, during which the turbulence fluxes evolve from 0 toward approximately quasi-steady state profiles. LES results that are obtained during the spin-up phase are typically ignored for analysis as they are artifacts of starting from a nonturbulent state. This example shows that the spin-up phase can have a significant impact on the evolution of horizontal winds. If the focus of an LES experiment is on horizontal winds, or anything that depends strongly on them, unwanted deviations that arise during the spin-up phase may be avoided by applying a nudging term. Otherwise, one might start the model with the winds set to their geostrophic values, as was done for CONSTRAIN case simulations reported by Schlemmer et al. (2017).

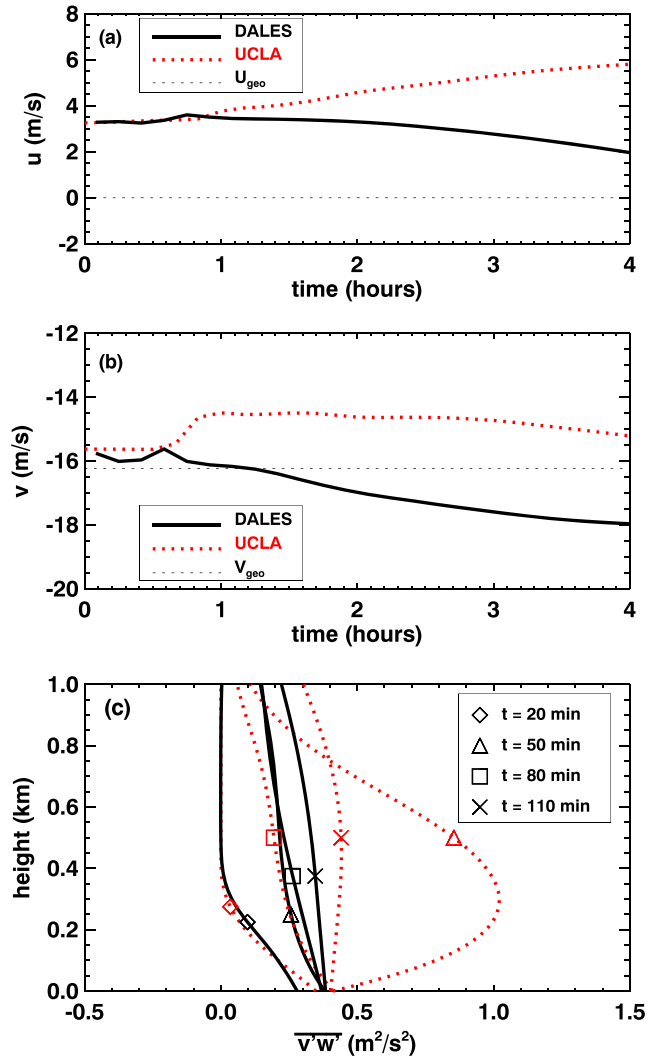

Figure A1. Time series of (a) u and (b) v at 500-m height as obtained from DALES and UCLA-LES for the reference case and the geostrophic wind velocity. The total fluxes of $\overline{v'w'}$ at four different times are displayed in (c). Line styles are according to the legends. The model names are given in Table 1.

Acknowledgments
The PALM simulations with DALES including ice were performed with resources provided by the North-German Supercomputing Alliance (HLRN) and the Deutsche Forschungsgemeinschaft (DFG, German Research Foundation)—Projektnummer 268020496—TRR 172, within the Transregional Collaborative Research Center "ArctiC Amplification: Climate Relevant Atmospheric and SurfaCe Processes, and Feedback Mechanisms $(AC)^3$." DHARMA simulations used resources provided by the NASA High-End Computing (HEC) Program through the NASA Advanced Supercomputing (NAS) Division at Ames Research Center. The case specifics are posted at the Met Office website (http://appconv.metoffice.com/cold_air_outbreak/constrain_case/home.html). The simulation data in this study are stored at the EUCLIPSE website (www.euclipse.nl/CONSTRAIN/model.tar), with `model` the (case sensitive) model name, DALES, DHARMA, MONC, Meso-NH, PALM, SAM, or UCLA.

References

Abel, S. J., Boutle, I. A., Waite, K., Fox, S., Brown, P. R. A., Cotton, R., et al. (2017). The role of precipitation in controlling the transition from stratocumulus to cumulus clouds in a Northern Hemisphere cold-air outbreak. *Journal of the Atmospheric Sciences*, *74*, 2293–2314. https://doi.org/10.1175/JAS-D-16-0362.1

Ackerman, A. S., Kirkpatrick, M. P., Stevens, D. E., & Toon, O. B. (2004). The impact of humidity above stratiform clouds on indirect aerosol forcing. *Nature*, *432*, 1014–1017. https://doi.org/10.1038/nature01174

Albrecht, B. (1989). Aerosols, cloud microphysics, and fractional cloudiness. *Science*, *245*, 1227–1230.

Arakawa, A., Jung, J., & Wu, C. (2011). Toward unification of the multiscale modeling of the atmosphere. *Atmospheric Chemistry and Physics*, *11*, 3731–3742.

Bengtsson, L., Andrae, U., Aspelien, T., Batrak, Y., Calvo, J., de Rooy, W., et al. (2017). The HARMONIE-AROME model configuration in the ALADIN-HIRLAM NWP system. *Monthly Weather Review*, *145*, 1919–1935.

Bogenschutz, P. A., & Krueger, S. K. (2013). A simplified PDF parameterization of subgrid-scale clouds and turbulence for cloud-resolving models. *Journal of Advances in Modeling Earth Systems*, *5*, 195–211. https://doi.org/10.1002/jame.20018

Boutle, I. A., Eyre, J. E. J., & Lock, A. P. (2014). Seamless stratocumulus simulation across the turbulent gray zone. *Monthly Weather Review*, *142*, 1655–1668.

Bretherton, C., & Blossey, P. (2017). Understanding mesoscale aggregation of shallow cumulus convection using large-eddy simulation. *Journal of Advances in Modeling Earth Systems*, *9*, 2798–2821. https://doi.org/10.1002/2017MS000981

Bretherton, C. S., Blossey, P. N., & Uchida, J. (2007). Cloud droplet sedimentation, entrainment efficiency, and subtropical stratocumulus albedo. *Geophysical Research Letters*, *34*, L03813. https://doi.org/10.1029/2006JD027648

Bretherton, C. S., & Wyant, M. C. (1997). Moisture transport, lower-tropospheric stability, and decoupling of cloud-topped boundary layers. *Journal of the Atmospheric Sciences*, *54*, 148–167.

Brümmer, B. (1999). Roll and cell convection in wintertime Arctic cold-air outbreaks. *Journal of the Atmospheric Sciences*, *56*, 2613–2636.

Cheng, A., & Xu, K.-M. (2008). Simulation of boundary-layer cumulus and stratocumulus clouds using a cloud-resolving model with low-and third-order turbulence closures. *Journal of the Meteorological Society of Japan*, *86A*, 67–86.

De Roode, S. R., Duynkerke, P. G., & Jonker, H. J. J. (2004). Large eddy simulation: How large is large enough? *Journal of the Atmospheric Sciences*, *61*, 403–421.

De Roode, S. R., Duynkerke, P. G., Jonker, H. J. J., & Stevens, B. (2004). Countergradient fluxes of conserved variables in the clear convective and stratocumulus-topped boundary layer: The role of the entrainment flux. *Boundary-Layer Meteorology*, *112*, 179–196.

De Roode, S. R. D., Jonker, H. J. J., van de Wiel, B. J. H., Vertregt, V., & Perrin, V. (2017). A diagnosis of excessive mixing in smagorinsky subfilter-scale turbulent kinetic energy models. *Journal of the Atmospheric Sciences*, *74*, 1495–1511.

De Roode, S. R., & Los, A. (2008). The effect of temperature and humidity fluctuations on the liquid water path of non-precipitating closed-cell stratocumulus. *Quarterly Journal of the Royal Meteorological Society*, *134*, 403–416.

De Roode, S. R., Sandu, I., van der Dussen, J. J., Ackerman, A. S., Blossey, P., Jarecka, D., et al. (2016). Large eddy simulations of EUCLIPSE/GASS lagrangian stratocumulus to cumulus transitions: Mean state, turbulence, and decoupling. *Journal of the Atmospheric Sciences*, *73*, 2485–2508.

Dearden, C., Hill, A., Coe, H., & Choularton, T. (2018). The role of droplet sedimentation in the evolution of low-level clouds over southern West Africa. *Atmospheric Chemistry and Physics*, *18*, 14253–14269.

Deardorff, J. W. (1980). Stratocumulus-capped mixed layers derived from a three-dimensional model. *Boundary-Layer Meteorology*, *18*, 495–527.

Dorrestijn, J., Crommelin, D. T., Siebesma, A. P., & Jonker, H. J. J. (2013). Stochastic parameterization of shallow cumulus convection estimated from high-resolution model data. *Theoretical and Computational Fluid Dynamics*, *27*, 133–148.

Duynkerke, P. G., Zhang, H.-Q., & Jonker, P. J. (1995). Microphysical and turbulent structure of nocturnal stratocumulus as observed during ASTEX. *Journal of the Atmospheric Sciences*, *52*, 2763–2777.

Field, P., Brozkova, R., Chen, M., Dudhia, J., Lac, C., Hara, T., et al. (2017). Exploring the convective greyzone with regional simulations of a cold air outbreak. *Quarterly Journal of the Royal Meteorological Society*, *143*, 2537–2555.

Field, P., Cotton, R., McBeath, K., Lock, A., Webster, S., & Allan, R. (2014). Improving a convection-permitting model simulation of a cold air outbreak. *Quarterly Journal of the Royal Meteorological Society*, *140*, 124–138.

Green, B. W., & Zhang, F. (2015). Numerical simulations of Hurricane Katrina (2005) in the turbulent gray zone. *Journal of Advances in Modeling Earth Systems*, *7*, 142–161. https://doi.org/10.1002/2014MS000399

Gryschka, M., Drüe, C., Etling, D., & Raasch, S. (2008). On the influence of sea-ice inhomogeneities onto roll convection in cold-air outbreaks. *Geophysical Research Letters*, *35*, L23804. https://doi.org/10.1029/2008GL035845

Gryschka, M., Fricke, J., & Raasch, S. (2014). On the impact of forced roll convection on vertical turbulent transport in cold air outbreaks. *Journal of Geophysical Research: Atmospheres*, *119*, 12,513–12,532. https://doi.org/10.1002/2014JD022160

Gryschka, M., & Raasch, S. (2005). Roll convection during a cold air outbreak: A large-eddy simulation with stationary model domain. *Geophysical Research Letters*, *32*, L14805. https://doi.org/10.1029/2005GL022872

Heus, T., van Heerwaarden, C. C., Jonker, H. J. J., Siebesma, A. P., Axelsen, S., van den Dries, K., et al. (2010). Formulation of the Dutch Atmospheric Large-Eddy Simulation (DALES) and overview of its applications. *Geoscientific Model Development*, *3*, 415–444.

Heymsfield, A. J., & Iaquinta, J. (2000). Cirrus crystal terminal velocities. *Journal of the Atmospheric Sciences*, *57*, 916–938.

Heymsfield, A. J., & Kajikawa, M. (1987). An improved approach to calculating terminal velocities of plate-like crystals and graupel. *Journal of the Atmospheric Sciences*, *44*, 1088–1099.

Honnert, R., Masson, V., & Couvreux, F. (2011). A diagnostic for evaluating the representation of turbulence in atmospheric models at the kilometric scale. *Journal of the Atmospheric Sciences*, *68*, 3112–3131.

Jonker, H. J. J., Duynkerke, P. G., & Cuijpers, J. W. M. (1999). Mesoscale fluctuations in scalars generated by boundary layer convection. *Journal of the Atmospheric Sciences*, *56*, 801–808.

Khairoutdinov, M. F., & Kogan, Y. L. (1999). A large eddy simulation model with explicit microphysics: Validation against aircraft observations of a stratocumulus-topped boundary layer. *Journal of the Atmospheric Sciences*, *56*, 2115–2131.

Khairoutdinov, M. K., & Randall, D. A. (2003). Cloud-resolving modeling of the ARM summer 1997 IOP: Model formulation, results, uncertainties and sensitivities. *Journal of the Atmospheric Sciences*, *60*, 607–625.

Kirkpatrick, M., Ackerman, A., Stevens, D., & Mansour, N. (2006). On the application of the dynamic Smagorinsky model to large-eddy simulations of the cloud-topped atmospheric boundary layer. *Journal of the Atmospheric Sciences*, *63*, 526–546.

Klein, S. A., McCoy, R. B., Morrison, H., Ackerman, A. S., Avramov, A., Boer, G. d., et al. (2009). Intercomparison of model simulations of mixed-phase clouds observed during the arm mixed-phase arctic cloud experiment. I: Single-layer cloud. *Quarterly Journal of the Royal Meteorological Society*, *135*, 979–1002.

Lac, C., Chaboureau, P., Masson, V., Pinty, P., Tulet, P., Escobar, J., et al. (2018). Overview of the Meso-NH model version 5.4 and its applications. *Geoscientific Model Development*, *11*, 1929–1969.

Lafore, J.-P., Stein, J., Asencio, N., Bougeault, P., Ducrocq, V., Duron, J., et al. (1997). The Meso-NH atmospheric simulation system. Part I: Adiabatic formulation and control simulations. *Annales Geophysicae*, *16*, 90–109. Springer.

Larson, V. E., Schanen, D. P., Wang, M., Ovchinnikov, M., & Ghan, S. (2012). PDF parameterization of boundary layer clouds in models with horizontal grid spacings from 2 to 16 km. *Monthly Weather Review*, *140*, 285–306.

Lebeaupin Brossier, C., Ducrocq, V., & Giordani, H. (2008). Sensitivity of three mediterranean heavy rain events to two different sea surface fluxes parameterizations in high-resolution numerical modeling. *Journal of Geophysical Research*, *113*, D21109. https://doi.org/10.1029/2007JD009613

Louis, J. F. (1979). A parametric model of vertical fluxes in the atmosphere. *Boundary-Layer Meteorology*, *17*, 187–202.

Malavelle, F. F., Haywood, J. M., Field, P. R., Hill, A. A., Abel, S. J., Lock, A. P., et al. (2014). A method to represent subgrid-scale updraft velocity in kilometer-scale models: Implication for aerosol activation. *Journal of Geophysical Research: Atmospheres*, *119*, 4149–4173. https://doi.org/10.1002/2013JD021218

Maronga, B., Gryschka, M., Heinze, R., Hoffmann, F., Kanani-Sühring, F., Keck, M., et al. (2015). The Parallelized Large-Eddy Simulation Model (PALM) version 4.0 for atmospheric and oceanic flows: Model formulation, recent developments, and future perspectives. *Geoscientific Model Development*, *8*, 2515–2551.

Morrison, H., Curry, J., & Khvorostyanov, V. (2005). A new double-moment microphysics parameterization for application in cloud and climate models. Part I: Description. *Journal of the Atmospheric Sciences*, *62*, 1665–1677.

Müller, G., & Chlond, A. (1996). Three-dimensional numerical study of cell broadening during cold-air outbreaks. *Boundary-Layer Meteorology*, *81*, 289–323.

Nakamura, K., Hara, M., Noda, A. T., Tomita, H., & Wakazuki, Y. (2012). Simulation and verification of tropical deep convective clouds

using eddy-permitting regional atmospheric models II. Earth simulator center annual rep: Japan Agency for Marine-Earth Science and Technology. Yokohama, Japan.

Neggers, R. A. J., Ackerman, A. S., Angevine, W. M., Bazile, E., Beau, I., Blossey, P. N., et al. (2017). Single-column model simulations of subtropical marine boundary-layer cloud transitions under weakening inversions. *Journal of Advances in Modeling Earth Systems*, *9*, 2385–2412. https://doi.org/10.1002/2017MS001064

Ovchinnikov, M., Ackerman, A. S., Avramov, A., Cheng, A., Fan, J., Fridlind, A. M., et al. (2014). Intercomparison of large-eddy simulations of Arctic mixed-phase clouds: Importance of ice size distribution assumptions. *Journal of Advances in Modeling Earth Systems*, *6*, 223–248. https://doi.org/10.1002/2013MS000282

Pinty, J., & Jabouille, P. (1998). A mixed-phase cloud parameterization for use in mesoscale non-hydrostatic model: Simulations of a squall line and of orographic precipitations, *Conf. on Cloud Physics* (pp. 217–220). Everett, WA: American Meteorological Society.

Pithan, F., Svensson, G., Caballero, R., Chechin, D., Cronin, T. W., Ekman, A. M., et al. (2018). Role of air-mass transformations in exchange between the Arctic and mid-latitudes. *Nature Geoscience*, *11*, 805.

Raasch, S., & Schröter, M. (2001). PALM—A large-eddy simulation model performing on massively parallel computers. *Meteorologische Zeitschrift*, *10*, 363–372.

Richter, I. (2015). Climate model biases in the eastern tropical oceans: Causes, impacts and ways forward. *Wiley Interdisciplinary Reviews: Climate Change*, *6*, 345–358. https://doi.org/10.1002/wcc.338

Salesky, S. T., Chamecki, M., & Bou-Zeid, E. (2017). On the nature of the transition between roll and cellular organization in the convective boundary layer. *Boundary-Layer Meteorology*, *163*, 41–68.

Sandu, I., Brenguier, J., Geoffroy, O., Thouron, O., & Masson, V. (2008). Aerosol impacts on the diurnal cycle of marine stratocumulus. *Journal of the Atmospheric Sciences*, *65*, 2705–2718.

Sandu, I., & Stevens, B. (2011). On the factors modulating the stratocumulus to cumulus transitions. *Journal of the Atmospheric Sciences*, *68*, 1865–1881.

Sandu, I., Stevens, B., & Pincus, R. (2010). On the transitions in marine boundary layer cloudiness. *Atmospheric Chemistry and Physics*, *10*, 2377–2391.

Savic-Jovcic, V., & Stevens, B. (2008). The structure and mesoscale organization of precipitating stratocumulus. *Journal of the Atmospheric Sciences*, *65*, 1587–1605.

Schlemmer, L., Bechtold, P., Sandu, I., & Ahlgrimm, M. (2017). Uncertainties related to the representation of momentum transport in shallow convection. *Journal of Advances in Modeling Earth Systems*, *9*, 1269–1291. https://doi.org/10.1002/2017MS000915

Schröter, J. S., Moene, A. F., & Holtslag, A. A. (2013). Convective boundary layer wind dynamics and inertial oscillations: the influence of surface stress. *Quarterly Journal of the Royal Meteorological Society*, *139*, 1694–1711.

Seifert, A., & Beheng, K. (2006). A two-moment cloud microphysics parameterization for mixed-phase clouds. Part 1: Model description. *Meteorology and Atmospheric Physics*, *92*, 45–66.

Shin, H. H., & Hong, S.-Y. (2013). Analysis of resolved and parameterized vertical transports in convective boundary layers at gray-zone resolutions. *Journal of the Atmospheric Sciences*, *70*, 3248–3261.

Stage, S. A., & Businger, J. A. (1981). A model for entrainment into a cloud-topped marine boundary layer. Part I. Model description and application to a cold-air outbreak episode. *Journal of the Atmospheric Sciences*, *38*, 2213–2229.

Stevens, B. (2002). Entrainment in stratocumulus-topped mixed layers. *Quarterly Journal of the Royal Meteorological Society*, *128*, 2663–2690.

Stevens, B., Cotton, W. R., Feingold, G., & Moeng, C. (1998). Large-eddy simulations of strongly precipitating, shallow stratocumulus-topped boundary layers. *Journal of the Atmospheric Sciences*, *55*, 3616–3638.

Stevens, B., Moeng, C.-H., Ackerman, A. S., Bretherton, C. S., Chlond, A., de Roode, S. R., et al. (2005). Evaluation of large-eddy simulations via observations of nocturnal marine stratocumulus. *Monthly Weather Review*, *133*, 1443–1462.

Tomassini, L., Field, P. R., Honnert, R., Malardel, S., McTaggart-Cowan, S., Saitou, K., et al. (2017). The "grey zone" cold air outbreak global model intercomparison: a cross-evaluation using large-eddy simulations. *Journal of Advances in Modeling Earth Systems*, *9*, 39–64. https://doi.org/10.1002/2016MS000822

Van der Dussen, J. J., de Roode, S. R., Ackerman, A. S., Blossey, P. N., Bretherton, C. S., Kurowski, M. J., et al. (2013). The GASS/EUCLIPSE model intercomparison of the stratocumulus transition as observed during ASTEX: LES results. *Journal of Advances in Modeling Earth Systems*, *5*, 483–499. https://doi.org/10.1002/jame.20033

Van der Dussen, J. J., de Roode, S. R., & Siebesma, A. P. (2014). Factors controlling rapid stratocumulus cloud thinning. *Journal of the Atmospheric Sciences*, *71*, 655–664.

Wang, H., & Feingold, G. (2009). Modeling mesoscale cellular structures and drizzle in marine stratocumulus. Part I: Impact of drizzle on the formation and evolution of open cells. *Journal of the Atmospheric Sciences*, *66*, 3237–3256.

Wood, R., & Hartmann, D. L. (2006). Spatial variability of liquid water path in marine low cloud: The importance of mesoscale cellular convection. *Journal of Climate*, *19*, 1748–1764.

Wyngaard, J. C. (2004). Toward numerical modeling in the "terra incognita". *Journal of the Atmospheric Sciences*, *16*, 1816–1826.

Yamaguchi, T., Feingold, G., & Kazil, J. (2017). Stratocumulus to cumulus transition by drizzle. *Journal of Advances in Modeling Earth Systems*, *9*, 2333–2349. https://doi.org/10.1002/2017MS001104

Zhou, X., Ackerman, A. S., Fridlind, A. M., & Kollias, P. (2018). Simulation of mesoscale cellular convection in marine stratocumulus. Part I: Drizzling conditions. *Journal of the Atmospheric Sciences*, *75*, 257–274.